

# We are IntechOpen, the world's leading publisher of Open Access books Built by scientists, for scientists

6,900

Open access books available

186,000

International authors and editors

200M

Downloads

Our authors are among the

154

Countries delivered to

TOP 1%

most cited scientists

12.2%

Contributors from top 500 universities



WEB OF SCIENCE™

Selection of our books indexed in the Book Citation Index  
in Web of Science™ Core Collection (BKCI)

Interested in publishing with us?  
Contact [book.department@intechopen.com](mailto:book.department@intechopen.com)

Numbers displayed above are based on latest data collected.  
For more information visit [www.intechopen.com](http://www.intechopen.com)



---

# Novel SNOM Probes Based on Nanofocusing in Asymmetric Structures

---

Valeria Lotito, Christian Hafner, Urs Sennhauser and Gian-Luca Bona

Additional information is available at the end of the chapter

<http://dx.doi.org/10.5772/50806>

---

## 1. Introduction

Scanning near-field optical microscopy (SNOM) has become a microscopy tool of paramount importance for nanostructure investigation in different fields ranging from material to life science. In fact, such technology combines the advantages offered by classical optical microscopy with high resolution typical of scanning probe microscopy (SPM) [1,2]. More specifically, it allows overcoming the diffraction limit by exploitation of the non-propagating evanescent waves in the near-field zone, which are not retrieved in conventional optical microscopy. Still it retains some important features of this technique, e.g. the possibility to carry out real time observation of the sample in its native environment in a non-invasive way and with little sample preparation and, more importantly, the availability of a wide variety of contrast mechanisms, like polarization, absorption and fluorescence. Such advantageous characteristics are usually not affordable with non-optical scanning probe techniques, which require more awkward sample preparation and provide little information on non-morphological properties of the sample. On the other hand, similarly to SPM, SNOM enables to get also high resolution information on sample topography by scanning a sharp probe in the region of interest of the sample and using a non-optical short range interaction between the probe and the sample to control probe-sample distance. Hence, SNOM allows getting nano-scale insight into a specimen, casting light on both topographic and optical properties of the sample.

As suggested by the name itself, optical properties of SNOM rely on the near-field interaction between the probe and the sample: the probe can be used for near-field excitation of the sample, whose response is collected in the far-field or to detect the near-field response of the sample broadly illuminated in the far-field or for both. Independently of the specific excitation/detection scheme, a crucial role in the ultimate attainable optical resolution is played by the probe itself, whose design, modelling and optimization has been

encouraged by a vast wealth of numerical methods, shedding light into the optical behaviour of the probe at very small scales.

The best known probe configuration, used by the pioneers of SNOM, is the so-called aperture probe, which is still commonly used today [1,3,4]. Such a structure is based on a metal-coated tapered dielectric (typically an optical fiber) with an aperture left at the very apex. In this case, resolution is mostly dictated by the size of the aperture, which cannot be decreased at will not only because of technological limits, but also due to the dramatic slump in signal throughput with decreasing aperture size. The latter cannot be simply improved by increasing the input power because of the potential risk for thermal damage. Significant heating can occur as a consequence of multiple back-reflections from the taper and metal absorption, resulting in aperture expansion, tip contraction and elongation, possible partial detachment or even breakdown of the metal layer due to mechanical stresses arising from the different thermal expansion coefficients of the fiber and the metal coating [1,5-7]. All these phenomena inherently cause degradation of the probe behaviour and impose severe limits on the injected power.

Another major factor influencing the performance of aperture probes is the taper cone angle. In fact, such probes can be viewed as a tapered hollow metal waveguide filled with a dielectric, in which the mode structure changes as a function of the characteristic dimension of the dielectric core [8]. Guided modes run into cut-off one after the other as the diameter decreases, until, at a well-defined diameter, even the last guided mode, the fundamental  $HE_{11}$  mode, runs into cut-off; for smaller diameters of the dielectric core, the energy in the core decays exponentially because of the purely imaginary propagation constant of all the modes [1]. The amount of light that reaches the probe aperture depends on the distance separating the aperture and the  $HE_{11}$  cut-off diameter: the larger the opening angle of the tapered structure, the better the light transmission of the probe is, as the final cut-off diameter approaches the probe apex [1].

Taper profile depends of course on the adopted fabrication method: for fiber-based probes, two main approaches are used for taper formation, either fiber heating and pulling (consisting in locally heating the fiber using a  $CO_2$  laser and subsequently pulling apart the two parts) and chemical etching (which basically consists in dipping the fiber in a HF solution with an organic overlayer) [1,2]. The second approach usually results in shorter tapers, i.e. larger opening angles, beneficial for higher signal throughput in spite of a higher surface roughness, which can be reduced by resorting to some variants of the etching process like the so-called tube etching process. Even shorter tapers can be achieved by using the selective etching methods in which the different etching rates of the core and the cladding of the fiber are exploited to get probes in which only the core of the fiber is tapered, resulting in tapered length of few micrometers against the hundreds of micrometers of fibers produced by different techniques. The following steps consist in metal deposition (by thermal or e-beam evaporation or sputtering) and aperture formation, which can be done either by exploiting shadowing effects during metal evaporation or by punching or with focused ion beam (FIB) milling [1].

Several attempts have been carried out to overcome the fundamental limitations of aperture probes, i.e. poor throughput and poor resolution. Two main routes have been followed to improve their performance, i.e. optimization of the taper profile and of the aperture shape.

As pointed out earlier, chemical etching leads to an advantageous reduction of the overall taper length and a better control of the overall taper shape. Using selective chemical etching, probes based on multiple tapers like the double taper, the triple taper and the steeple-on-mesa taper profiles have been realized: the goal of these structures was to benefit from the advantages of large taper angles in signal throughput at least for part of the probe because the use of a single taper with a large taper angle would not be convenient during approach to the sample [9-13]. An asymmetric edged probe with a sharp edge at the foot of the conical taper has shown to improve the transmission of  $HE_{11}$  mode with proper linearly polarized excitation along the direction of the asymmetry [14]. Also the taper profile of probes produced by heating and pulling has been optimized: for this fabrication process the overall probe profile can be varied by controlling some process parameters; parabolic profiles have shown to give rise to higher throughput compared to conical profiles [15]. Theoretical studies have been carried out to assess the influence of taper profile on probe performance to determine optimal shapes in terms of throughput: for example, structures based on the alternation of conical and cylindrical sections or analytical expressions for improved taper profiles have been proposed as well as corrugations at the interface between the dielectric core and the metal coating or on the external metal coating; in the latter two cases, the increase in the throughput is due to the exploitation of surface plasmon polaritons (SPPs) [16-19].

Another route followed for the improvement of the performance of aperture probes has been the implementation of other aperture shapes different from the typical circular design: rectangular, square, slit, elliptical, C-shaped, I-shaped or dumbbell, H-shaped, bowtie, connected and separated double aperture, triangular, rod hole and tooth hole, gap apertures have been analysed and/or fabricated in fiber- and cantilever-based probes [20-28]. The improved throughput and field localization for some preferential input polarizations is due to the strong asymmetry of such aperture shapes and to the excitation of SPPs.

Despite the efforts in the optimization of the aperture probe to overcome its fundamental limits in throughput and resolution, the current design of aperture probes is not able to sustain routinely ultrahigh resolution imaging because of the limit of the skin depth of the metal coating that increases the effective aperture size, thus making the field distribution at the aperture significantly larger than its physical size [29]. Better throughput and resolution are expected if an apertureless metal or fully metal-coated probe is used, due to the combination of electrostatic lightning rod effect and surface plasmon excitation for proper illumination conditions. For example, due to the lightning rod effect, strong enhancement is expected at the tip apex, even though a real probe apex does not represent a real singularity (i.e. not defined first and second order derivatives) because of the finite conductivity of real metals and the finite tip radius [29]. In the next paragraph, we will see how plasmonic effects in apertureless probes can be used to get high resolution.

## 2. Nanofocusing in SNOM probes: The axisymmetric structure

Apertureless probes represent a promising alternative probe configuration. The fundamental problem with such probes is given by the fact that they are usually illuminated externally either by a focusing lens or using a prism-based total internal reflection configuration, resulting in a strong background due to far-field illumination, which could be detrimental for some sensitive samples and can be reduced only partially by on-axis illumination [30]. In order to reduce such background some groups have envisaged different solutions like far-field excitation of SPPs at the wide end of a tapered metal nanowire by using grating geometry: such SPPs propagate towards the apex of the nanowire leading to nanofocusing, that is delivery and concentration/focusing of the optical energy at the nanoscale, which means a region much smaller than the dimensions allowed by the diffraction limits [30,31].

Nanofocusing in metal tapered nanorods has been theoretically studied starting from the analysis of the SPP modes of a plasmonic waveguide consisting of a metal nanowire whose axis coincides with the  $z$  axis and whose dielectric function  $\epsilon_m(\omega)$  is uniform in space with  $\omega$  being the excitation angular frequency; the wire is surrounded by a dielectric with dielectric function  $\epsilon_d$  [31]. The three fundamental SPP modes supported by a metal nanowire are the transverse magnetic TM mode and two hybrid modes HE<sub>1</sub> and HE<sub>2</sub> (Figure 1). Note that we adopted this notation to indicate the modes, although the classification in TM<sub>0n</sub> (or TM<sub>n</sub>), TE<sub>0n</sub> (or TE<sub>n</sub>), HE<sub>mn</sub>, EH<sub>mn</sub> (where  $m$  is related to the angular symmetry and  $n$  to the radial variation of the mode) commonly used for circular dielectric wires might still be extended to circular metallic wires. Moreover, we considered the modes with lower losses.

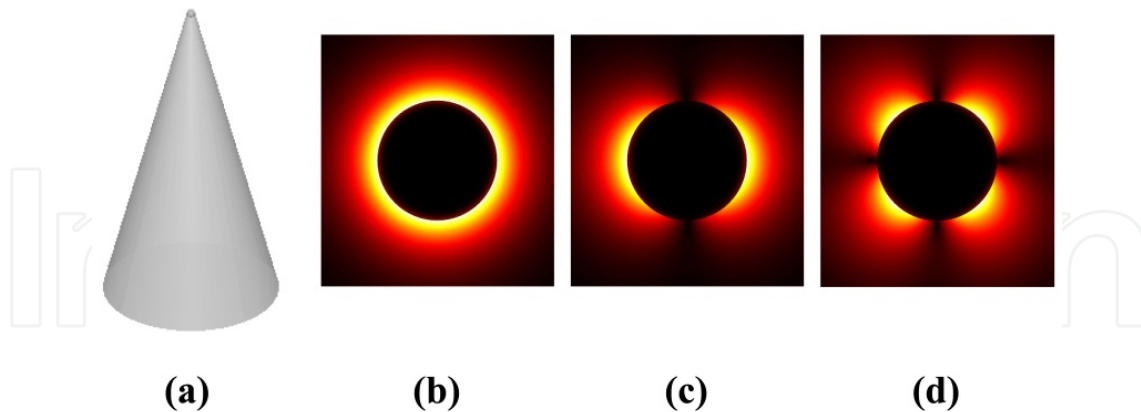


**Figure 1.** Sketch of: (a) fully metal probe; normalized electric field distributions of (b) TM plasmon mode, (c) HE<sub>1</sub> plasmon mode, (d) HE<sub>2</sub> plasmon mode.

The TM SPP mode can exist for arbitrarily small diameters of the nanowire and, hence, has been shown to be suitable for nanofocusing. This mode is axially uniform and is characterized by a magnetic field having only  $\phi$  component; both electric and magnetic fields are independent of  $\phi$ . Assuming that the radius  $R(z)$  of the nanowire is a smooth function of  $z$  (which decreases from microscale to nanoscale for  $z$  going from large negative

values to zero), the so-called eikonal or Wentzel-Kramers-Brillouin (WKB) or quasi-classical or geometric optics approximation can be applied to study the SPP modes and back-reflections can be neglected [31]. In order to study their propagation in a tapered metal rod, one can use a staircase approximation and interpret the taper as a series of cylindrical nanowires with smoothly decreasing diameters. The effective index  $n_{eff}(R) = n_{eff}(R(z))$  for the TM mode of the plasmonic waveguide at a point  $z$  can be determined from:

$$\left[ \frac{\varepsilon_d}{\kappa_d} \frac{K_1(\kappa_d R)}{K_0(\kappa_d R)} + \frac{\varepsilon_m}{\kappa_m} \frac{I_1(\kappa_m R)}{I_0(\kappa_m R)} \right] = 0 \quad (1)$$

where  $I_n$  and  $K_n$  are the modified Bessel functions of the first and second kind,  $\kappa_d = k_0 \sqrt{n_{eff}^2 - \varepsilon_d}$  and  $\kappa_m = k_0 \sqrt{n_{eff}^2 - \varepsilon_m}$ . Under the plasmonic condition  $\text{Re}\{\varepsilon_m\} < -\varepsilon_d$ , one gets the solutions for the SPP modes. For a thick wire ( $k_0 R \gg 1$ ), the solution is the same as for a flat surface:

$$n_{eff} = \sqrt{\frac{\varepsilon_m \varepsilon_d}{\varepsilon_m + \varepsilon_d}} \quad (2)$$

For a thin, nano-scale radius wire ( $k_0 R \ll 1$ ) one gets approximately with logarithmic precision [31]:

$$n_{eff}(R) \approx \frac{1}{k_0 R} \sqrt{-\frac{2\varepsilon_d}{\varepsilon_m}} \left[ \ln \sqrt{-\frac{4\varepsilon_m}{\varepsilon_d}} - \gamma \right]^{-1} \quad (3)$$

where  $\gamma \approx 0.57721$  is the Euler constant. From the previous expression it can be inferred that at the tip ( $k_0 R \rightarrow 0$ ),  $n_{eff} \rightarrow \infty$ ; therefore, the wave number increases and the SPPs asymptotically stop as both the phase and group velocity tend to zero because they are both proportional to  $k_0 R$  [31]. Besides, the study of the propagation of the SPPs through the tapered metal rod carried out with the staircase approximation has revealed an anomalous increase in the SPP field amplitudes, as SPPs approach the tip, because the electric field varies as  $\propto R^{-\frac{3}{2}}$  [32]. As a consequence, the simultaneous wavelength decrease and amplitude increase lead to a concurrent energy localization and, hence, to nanofocusing. Several theoretical studies have shown such a phenomenon [32-35]. The TM SPP mode can be excited using an axially symmetric grating under radially polarized excitation [36,37] or double-sided E-symmetric excitation [38] or asymmetric excitation via grating coupling on just one side of the tip [39].

An even more promising solution compared to fully metal probes in terms of simplification of the experimental set-up is the excitation of SPP modes on the metal coating of a fully metal-coated dielectric probe used under internal back excitation [29,40].

As for fully metal probes, the adiabatic approximation has been used to evaluate analytically the wave propagation in the fully metal-coated tapered dielectric probe, considering the cone as a succession of cylinders made up of a dielectric core of radius  $r_1$  surrounded by a metal coating of thickness  $\delta$  located in its turn in a dielectric medium [41]: in a first approximation, waveguide modes (WGM) have been calculated as those supported by a dielectric core surrounded by an infinitely thick metallic coating neglecting the external dielectric, while SPP modes have been calculated as those supported by a metal wire surrounded by a dielectric neglecting the internal dielectric core. Dispersion relations for waveguide modes and for SPP modes have thus been determined (the latter coincides with the dispersion equation for the metal wire). At a certain value of  $r_1$ , the wavevector of the WGM can match the one of the SPP mode: in these conditions, energy transfer from the WGM into the SPP mode is possible and, as a result, surface plasmons are excited bringing about nanofocusing. The transfer of energy and the field profiles can be determined with this approach using the coupled mode theory [41,42]. In this way, the SPPs can be excited using the WGM, thereby overcoming the problem of background inherent in the use of fully metal probes under external illumination.

The energy transfer from WGM to SPP modes has been thoroughly investigated in several studies, taking into account not only the “outer” SPP modes at the outer metal surface, but also the “inner” SPP modes at the inner metal surface; in some studies, non-conical taper profiles have been scrutinized as well [40,43-45]. The WGM has to present proper characteristics in order for the excited surface plasmons to exhibit axial symmetry, thereby interfering constructively at the tip apex and therefore generating nanofocusing. The three fundamental WGMs are a pair of orthogonal linearly polarized modes followed by a radially polarized one. If the fully metal-coated structure is excited by a linearly polarized  $HE_{11}$  mode, then the electric fields of the excited surface plasmons have opposite polarities on the opposite sides of the probe, giving rise to destructive interference at the very end of the probe; on the contrary, a radially polarized WGM excites SPPs with axial symmetry, which interfere constructively at the tip apex. These mechanisms are responsible for the high field confinement in case of radially polarized excitation compared to the linearly polarized case. The eventual outcome of this process is the creation of an ultrasmall hot spot in the region close to the tip apex in the former situation, as opposed to broader and weaker two-lobed electric field intensity distributions for the latter one. In particular, the size of the achievable hot spot in case of radially polarized excitation (and, hence, the ultimate attainable resolution) is mostly limited by the diameter of the metal apex, which can be decreased at will. Such behaviour has been confirmed in both theoretical and experimental studies [29,40,46-50] and is sketched in Figure 2.

Because of its attractive characteristics, the fully metal-coated dielectric probe has been chosen as the starting point for structural optimization; as explained in more detail in the next paragraph, the goal of the work will be the achievement of field localization (a feature of utmost importance for SNOM applications) under linearly polarized excitation, bringing about a further substantial simplification in experimental set-ups.

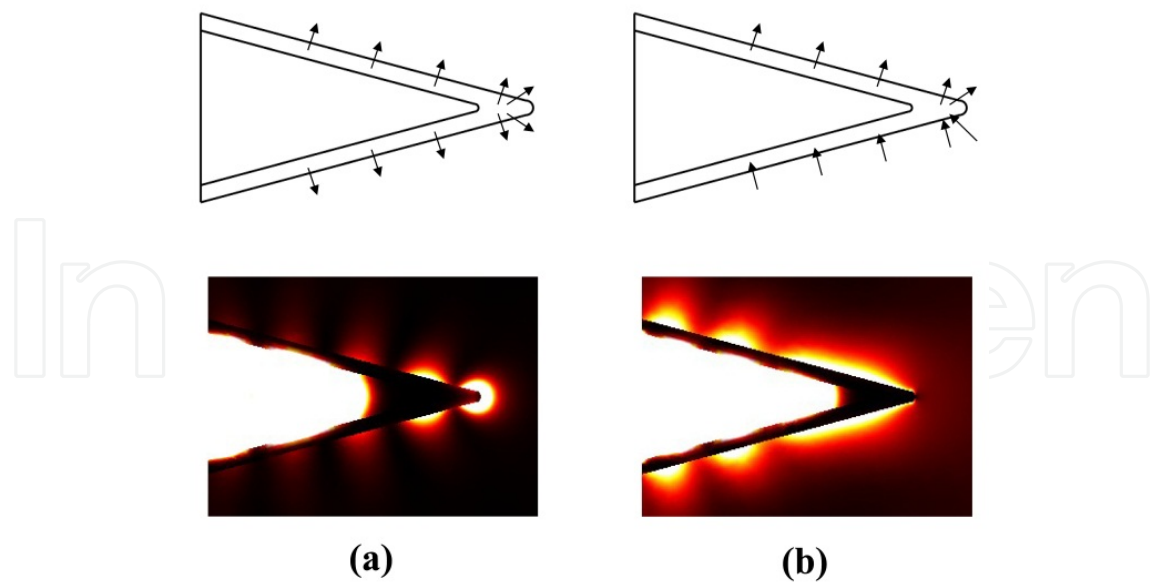


**Figure 2.** Sketch of the behaviour of a fully metal-coated dielectric probe under: (a) radially; (b) linearly polarized excitation. Arrows indicate the electric fields associated with the surface plasmons (adapted from [46]).

### 3. Nanofocusing in SNOM probes: The asymmetric structure

As previously explained, axisymmetric fully metal-coated probes under internal back excitation hold the promise for high-resolution applications, as they can allow the achievement of a strongly localized hot spot, whose size is mostly limited by the diameter of the metal apex, which can be decreased at will. However, as pointed out, the resolution of fully metal-coated tips is highly sensitive to the polarization state of the input field: such desirable field localization properties are affordable only under radially polarized excitation.

The reason for the strong polarization-dependent behaviour is due to the different characteristics of the surface plasmons excited by the different waveguide modes on the external metal coating: those excited by a linearly polarized mode interfere destructively at the tip apex, resulting in a weak and broad near-field distribution contrarily to those excited by a radially polarized mode which interfere constructively bringing about field localization.

The fundamental drawback of radially polarized excitation, despite its potential attractiveness, resides in its cumbersome injection procedure, which is extremely sensitive to misalignments that could impair the potential benefits stemming from its use [50,51].

In order to get similar superfocusing effects under a more easily excitable linearly polarized mode, one could break the axial symmetry of the fully metal-coated probe so as to avoid the destructive interference between the SPPs excited by a linearly polarized mode on the opposite sides of the axisymmetric structure. If  $z$  is the direction of the probe axis and an

asymmetry is introduced in the tip structure along  $x$ , field confinement under  $x$  linearly polarized mode could be expected. This idea stems from the numerical investigation of the effects of unintentional asymmetries like single and multiple air spherical bubbles, which have been shown to have a weak field localization effect due to the coupling between the linearly polarized mode along the direction of the asymmetry and the radially polarized one [52].

Of course, superfocusing based on random defects could not be easily forecast, but stronger and more easily predictable focusing effects can be achieved by the introduction of intentional modifications. The asymmetry can be either present in the probe structure itself or in the probe illumination scheme. Unilateral and bilateral slits in the metal coating have been numerically studied as a form of structural modification. Tip on aperture probes and probes based on a monopole antenna can also be included in this category [53,54]. An asymmetric illumination scheme can be used as an alternative to a structural asymmetry [55]: surface plasmons are excited only on one side of an apertureless probe via an opening close to the probe base in the offset aperture probe [56], while asymmetric single-sided SPP excitation results in field localization in an axisymmetric apertureless probe [38].

We have to underline how all these asymmetric structures are based on the introduction of an asymmetry along one specific direction and, for this reason, we can indicate them as “directional” asymmetries [55,57]. Hence, field localization occurs only for the linearly polarized mode that is oriented in the direction of the asymmetry: for example, if the asymmetry in the structure or in the illumination is along  $x$ , field localization is expected under  $x$  linearly polarized excitation, but not under  $y$  linearly polarized excitation, because no asymmetry is present along the  $y$  direction. This is due to the fact that all these forms of asymmetries exhibit a plane of symmetry and, hence, cannot guarantee field localization for arbitrarily oriented linearly polarized modes. Such asymmetries still require alignment between the linearly polarized mode and the asymmetry itself, even though injection procedures are considerably simplified because radially polarized excitation is no longer necessary.

The practical implication of such a behaviour in experimental applications is apparent if considering the difference in imaging properties using asymmetric tips based on a tip-on-aperture and on a monopole antenna grown on the rim of an aperture tip with different orientation of the input linear polarization, with dramatic variations in resolution and signal intensity upon rotation of the input excitation from the direction of the asymmetry to the orthogonal one [53,54]. However, the control of the direction of the input polarization is not an easy task and often imposes a determination *a posteriori* of the effective polarization direction close to the asymmetry by comparison of the field distribution observed close to the tip apex with simulation results [14].

Therefore, it would be desirable to attain superfocusing effects for arbitrarily oriented linearly polarized excitation, by using an “adirectional” asymmetry, which means a suitable modification likely to create an asymmetry along all spatial directions [55,57].

In the coming paragraphs, we will report the numerical analysis of novel forms of asymmetry based both on new types of structural directional asymmetries and on the pioneering concept of adirectional design. In particular, we will illustrate the properties of:

1. directional asymmetries based on: (i) an oblique cut; (ii) asymmetric corrugations in the metal coating;
2. adirectional asymmetries based on: (i) a spiral corrugation; (ii) azimuthal corrugations arranged in a spiral-like fashion.

Before tackling the design and the characteristics of these specific structures, in the next paragraph a short overview of the issues and difficulties encountered in probe modelling is presented.

#### **4. Optimization of probe structures: Challenges of tip modelling**

The theoretical study of the behaviour of SNOM probes is essential not only to get insight into the characteristics of commonly used probe structures and identify potential problems in imaging, but also to detect possible routes for optimization and predict the implications of the use of novel probe configurations. With such an approach, experimental efforts can be devoted to those probes that theoretically exhibit the most promising features.

Analytical solutions have been determined by Bethe and Bouwkamp for an aperture in an infinitely thin perfectly conducting screen, which laid down the foundation for further theoretical treatments. In the search for a model that could describe more faithfully the aperture probe behaviour, analytical studies that took into account the finite thickness of the metal screen have been carried out [58-59]. All of these treatments, however, suffer from neglecting the finite conductivity of the metal cladding used in real SNOM probes and provide little resemblance to the actual tip geometries used in experiments [60].

Other semi-analytical approaches have been based on a staircase approximation in which the longitudinally non-uniform waveguide (the tapered part of the probe) is considered as a succession of cylindrical sections of decreasing radius and the eigenmodes of the uniform waveguides obtained by infinitely stretching along the axis of the probe at each cross section are computed, as illustrated earlier. An analytical evaluation of the power transmitted by an aperture probe based on such an approximation using a mode matching theory has been done [1]. Starting also from this staircase approximation, different probe profiles like parabolic, exponential and mixed shapes based on the alternation of conical and cylindrical sections along the taper have been examined using the cross-section method [16, 17].

As discussed in paragraph 2, the staircase approximation has also been used for the analysis of nanofocusing in fully metal and fully metal-coated dielectric probes using local mode theory in a weakly non-uniform optical waveguide and the eikonal approximation [31, 34, 40, 43, 44].

Although analytical expressions are useful to get an understanding of probe behaviour, their range of applicability is limited. For example, the eikonal approximation can be applied as long as the adiabatic criterion is satisfied, i.e. for small local taper angles

[31,34,40,43]. On the other hand, the study of probes that do not satisfy such requirement can be of great interest: for example, optimal conditions for nanofocusing on tapered metal rods have been found in nonadiabatic conditions, which fail to be treated analytically [61]. Moreover, analytical methods turn out to be not adequate to model abrupt variations in the tapered profile as they often suppose a weak longitudinal non-uniformity.

Whenever more challenging probe geometries need to be studied, a numerical approach becomes mandatory. For this reason, the development of optimized probe structures has been accompanied and favoured by the flourishing of a vast range of numerical methods giving a glimpse at nanoscale mechanisms [9,62-64].

Such methods have been extensively used to investigate novel aperture shapes using, for example, the finite difference time domain method (FDTD) or the field susceptibility technique and in most of the cases considering apertures in thin metal films [21,24,26-28]. Furthermore, the analysis of wave propagation in tapered structures (either traditional conical tapers or structures modified with corrugations or multiple tapers) with an aperture at the end has been carried out using the finite difference beam propagation method [65], the FDTD method [18,19], the body of revolution FDTD method (BOR-FDTD) [48], the multiple multipole method (MMP) [66]. Fully metal probes and fully metal-coated pyramidal probes with different shapes have also been analysed both in case of direct illumination at the metal apex or with far-field excitation further away from the metal apex as described in paragraph 2 [36,37,61,67] using FDTD, BOR-FDTD, finite integration technique (FIT), and the finite element method (FEM). The fully metal-coated dielectric structure which, as anticipated, is the one of interest in this chapter, has been intensively numerically investigated especially under internal back excitation and its polarization-dependent properties have been carefully examined: the need for a radially polarized excitation has been pointed out as essential to get field localization [40,46-50].

Even numerical treatment is challenging because near-field probes involve different length scales: while phenomena of major interest for near-field interactions occur in the mesoscopic (sizes of the order of the incident wavelength) and nanoscopic (structures smaller than 100 nm) regimes [63], the overall probe structure, especially for fiber-based probes, can include sections much bigger than the incident wavelength. Computational cost for modelling a probe in its entirety would become prohibitive. Therefore, the overall computational domain is typically restricted to the very end of the probe, often using two-dimensional approximations or exploiting symmetry properties of the structure.

In the light of the previous considerations, we have investigated our novel probes based on appropriate modifications introduced in fully metal-coated dielectric probes adopting a numerical approach and restricting the analysis to the very end of the probe. An overview of the numerical approach adopted for our simulations is provided in the next paragraph, together with the description of the developed computational model. The model has been tested first to study the behaviour of the fully metal-coated probe, which, as reported in paragraph 2, has been already numerically and experimentally investigated and represents the reference for comparison for the new probe configurations.

## 5. Description of the computational model

Among the different numerical methods used in the past to simulate fully metal-coated SNOM probes, ranging from the MMP [46,68], to FIT [40,49,50,52,69], or the FDTD method [48], we have preferred FEM, chosen also in [47].

FEM is a tool used for the solution of differential equations in many disciplines, ranging from electromagnetics to solid and structural mechanics, from fluid dynamics to acoustics and thermal conduction [70]. A point of strength of FEM is its ability to deal with a complex geometry. Unstructured grids can accommodate for complex geometries in a much more straightforward way than other methods using Cartesian grids like finite difference methods.

The irregular domain is discretized into smaller and regular subdomains, known as finite elements, thereby replacing a domain having an infinite number of degrees of freedom by a system with a finite number of degrees of freedom. The essential principle behind FEM is a piecewise approximation: the solution of a complex problem is obtained by splitting the region of interest into smaller regions and approximating the solution over each subregion by a simple function [71].

In particular, our three-dimensional (3D) computational model for the simulation of the electromagnetic modes in the investigated probe configurations has been developed with the help of a commercial software (Comsol Multiphysics) based on FEM. The computational process is articulated in a two-dimensional (2D) analysis to calculate the eigenmodes at the input port, followed by the 3D simulation of the propagation of the first three eigenmodes, i.e., the two lowest order linearly polarized modes and the radially polarized one. Second order elements with minimum size of about 0.8 nm have been used. Simulations have been run on a 64 bit workstation with 32 GB of RAM.

The first examined structure is the fully metal-coated dielectric probe under radially and linearly polarized excitation. Although in this case one could benefit from the symmetry properties of the structure, the axisymmetric probe represents only the starting point for the search of optimized configurations, illustrated in the following paragraphs. As we will see, such structures are characterized by strong asymmetries, which impose the need for full 3D analysis. Therefore, for the sake of a better comparison, a 3D modelling has been adopted also for the reference axisymmetric structure, without resorting to any of the simplifications used in previous works to handle axially symmetric structures. Only the very end of the tip is examined due to the high computational burden of the simulations because of the different scales of the metal layer and the dielectrics. In previous works, simulations involving larger portions could be carried out only when the structure was less computationally challenging due the rotational symmetry of the probe allowing reduction of the problem complexity either with the BOR-FDTD method or even with approximate 2D simulations [18,48].

Figure 3 reports the sketch of the simulated axisymmetric probe, consisting of a silica core ( $n=1.5$ ) surrounded by an aluminium coating ( $n=0.645+5.029i$  at the operating wavelength

$\lambda=532$  nm). The radii of the inner silica cone and of the outer metallic hollow cone are 225 nm and 275 nm, respectively. Both cones (having an apex angle of  $30^\circ$ ) are rounded, with the radius of curvature of the inner cone being 10 nm, the one of the outer cone amounting to 20 nm. The overall modelling domain is a  $1.6 \mu\text{m}$  cylinder with radius  $1 \mu\text{m}$ . The probe axis lies on the  $z$  axis.

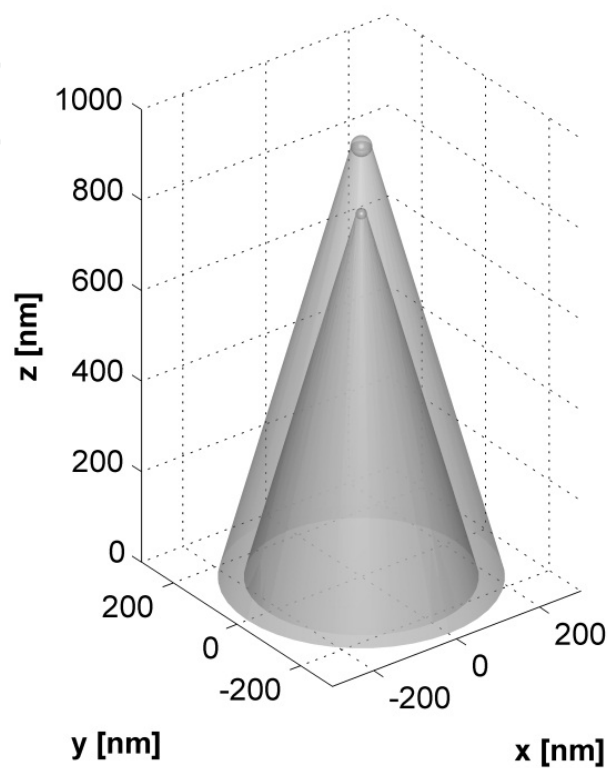


**Figure 3.** Sketch of the simulated axisymmetric fully metal-coated dielectric probe.

In Figure 4, the first three eigenmodes, i.e. the two lowest order  $x$  and  $y$  linearly polarized modes (H and V) and the radially polarized one (R), are reported together with the corresponding near-field distributions (square of the norm of the electric field) taken over a square area  $600 \text{ nm}$  by  $600 \text{ nm}$  centred around the probe apex at  $10 \text{ nm}$  from the apex; normalization to the maximum value of the electric field intensity distribution for the radial polarization has been done in order to emphasize the relative field strengths [51].

A highly localized hot spot with a full width at half maximum (FWHM) of  $38 \text{ nm}$  is observed for the R mode due to the constructive interference of the surface waves along the taper. As shown in [49], the size of the hot spot is influenced by the final rounding in the metal coating that, in our simulations, was chosen to be  $20 \text{ nm}$  in radius just for convenience as a reference for comparison and can be decreased at will. On the contrary, destructive interference of surface waves at the tip apex gives rise to two-lobed distributions, polarized mainly along the  $x$  and  $y$  axis, under H and V linearly polarized excitation, respectively; the average size (measured as the distance over which the field is more than or equal to half of its peak value) is approximately  $400 \text{ nm}$  and the peak value is about 50 times smaller than the peak of the R spot.

These results, in agreement with those previously obtained for such a probe, represent the reference for comparison for the novel probe configurations scrutinized in the following paragraphs, in which the characteristics of the near-field distributions at 10 nm from the apex of the modified probes are normalized to the peak value obtained in the axisymmetric probe under R excitation for an easier comparison.

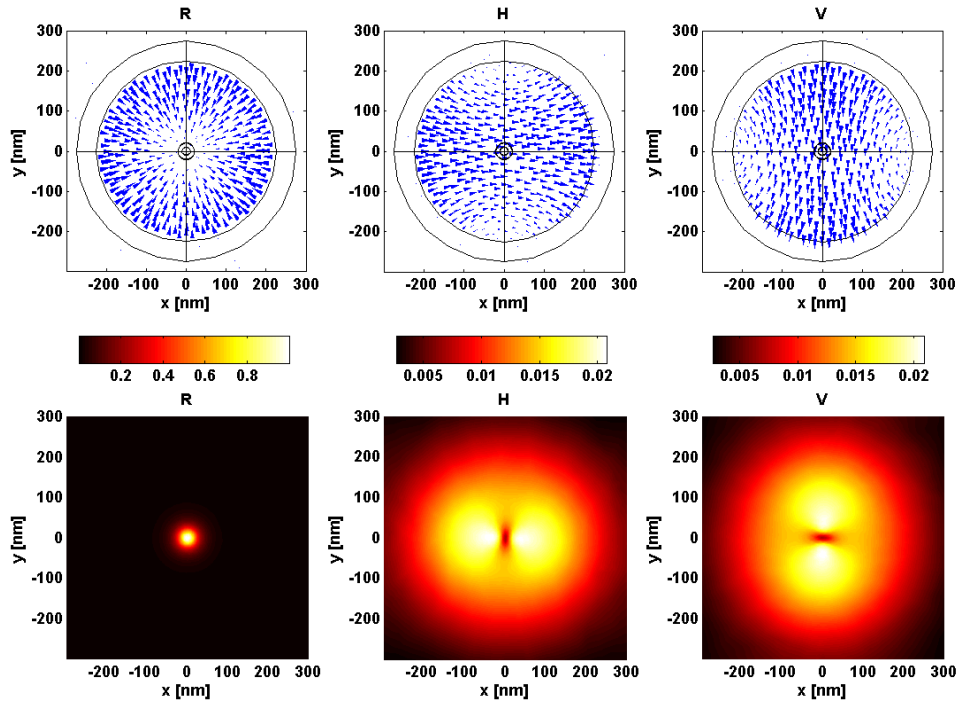


**Figure 4.** Illustration of input modes (upper row) and corresponding normalized near-field distributions at 10 nm from the apex of a standard axisymmetric fully metal-coated probe (lower row) (adapted from [51]).

## 6. Numerical investigation of probes with directional asymmetries under linearly polarized excitation

As anticipated, we have designed and investigated the behaviour of two different structural modifications that can be classified as directional asymmetries, one based on an oblique cut close to the tip apex stripping off both the metal coating and the inner core, and the other consisting of asymmetric corrugations in the metal coating. The sketches of the two structures are reported in Figure 5.

The first tip (Figure 5(a)) is cut along a plane which is neither orthogonal nor parallel to the tip axis: the cut angle (defined as the angle between a plane orthogonal to the axis of the tip and the plane of the cut itself) and the cut height (meant as the height of the new tip apex after the cut, measured from the bottom of the computational domain) can be varied [72].

The structure with asymmetric corrugations (Figure 5(b)) is based on the introduction on the outer metal surface of semicircular corrugations (either bumps or grooves), modelled by joining five truncated toroids of radius 20 nm with hemispherical terminations having the

same radius: the toroidal sections are filled with air in case of a groove or with metal in case of a bump [51]. The case of metal oxide filling has been considered as well. Corrugations are limited to just one half of the tip, hence their angular extension is less than  $180^\circ$ .

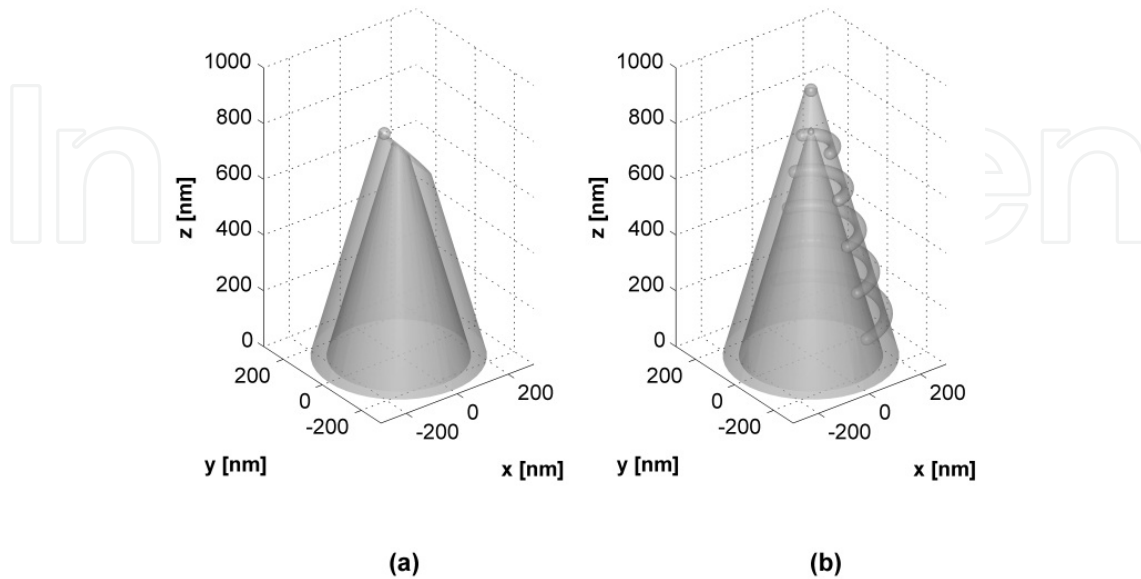


**Figure 5.** Sketch of the simulated structures based on an adirectional asymmetry: (a) probe with oblique cut; (b) asymmetrically corrugated fully metal-coated probe.

In both the cases, the asymmetry is present along the  $x$  direction.

### 6.1. Probe with oblique cut

For this probe structure, the behaviour of the probe under variable cut angle at constant cut height and for variable cut height at constant cut angle has been analysed [72].

In the first case, the angle has been varied from  $20^\circ$  to  $60^\circ$  (with a step of  $10^\circ$ ) at a height of 816 nm. Normalized near-field patterns under H and V polarized excitation are shown in Figure 6.

As expected, field localization is achieved only under H polarized excitation. The two initially separated lobes of the V mode tend to merge as the angle becomes steeper until getting completely intermingled, while the initially asymmetric spots obtained under H excitation become progressively more symmetric about their centre along the  $x$  axis as the cut angle increases. The FWHM and the peak value normalized to the one obtained in an axisymmetric probe under radially polarized excitation are reported in Figure 7 as a function of the cut angle. No dramatic changes occur in the size of the spots (always between 37 nm and 41 nm), while an increase in the H peak occurs with steeper cut angles.

A similar analysis carried out for a cut height varying from 741 nm to 841 nm (with a step of 25 nm) at a cut angle of  $30^\circ$  revealed once again field localization under H polarized excitation. The results of the simulations with variable cut height suggest the use of cuts involving a larger fraction of the originally axisymmetric probe because both the FWHM

and the peak value of the achieved hot spot undergo deterioration with increasing cut height. However, the approach to samples with steeper topographic variations would be hampered by cuts at lower heights unless a large cut angle is used at the same time, imposing a trade-off with the quality of the achievable H hot spot in the choice of the cut height.

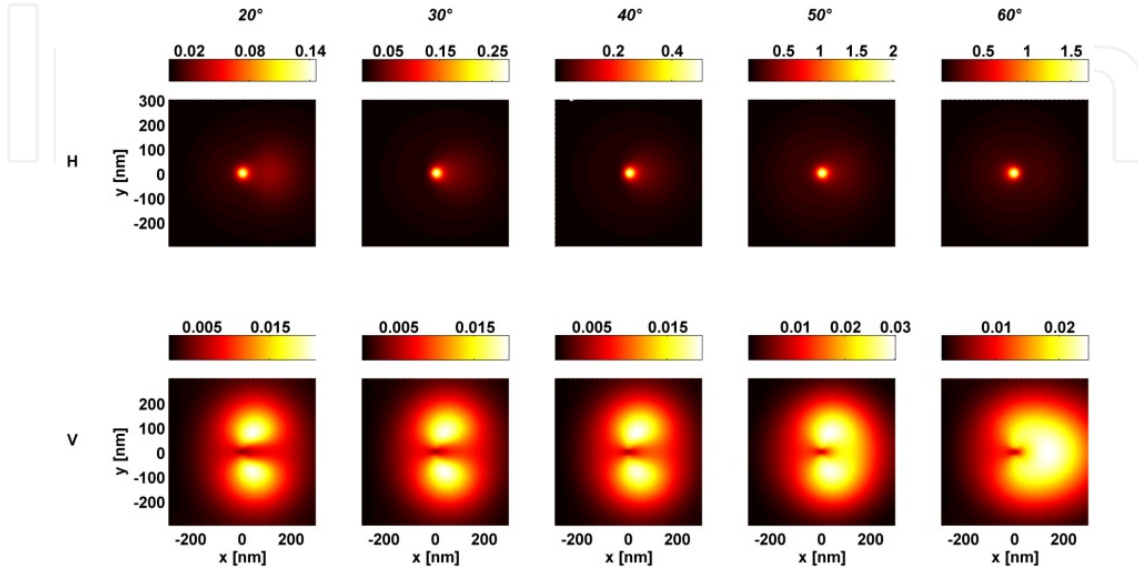


**Figure 6.** Normalized near-field intensity distributions at 10 nm from the apex of a cut probe with cut height of 816 nm and cut angle variable from 20° to 60° under H (upper row) and V (lower row) excitation (adapted from [72]).

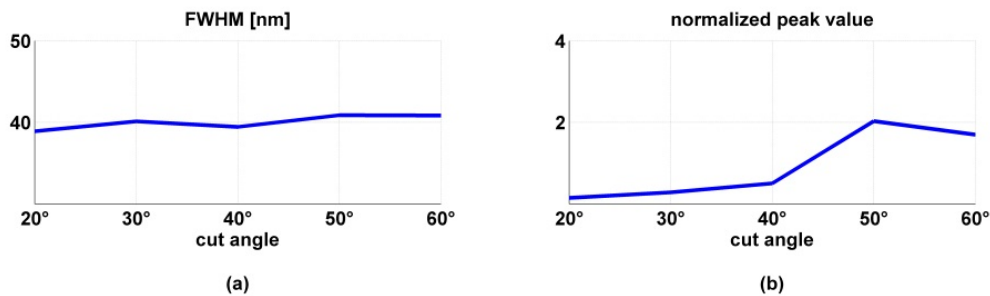


**Figure 7.** Characteristics of the near-field intensity distributions at 10 nm from the apex of the cut probe under H polarized excitation for variable cut angle: (a) FWHM; (b) peak value normalized to the one achieved in an axisymmetric probe under radially polarized excitation (adapted from [72]).

## 6.2. Probe with asymmetric corrugations

As we said, the five corrugations could consist in either grooves or bumps on the outer metal coating and are equally spaced, with the z-spacing amounting to 150 nm and the first bottom one centred at 150 nm from the input port [51].

First, the effect of a variation in the sequence of grooves and bumps has been considered and all the possible permutations of air indentations and metal bumps for the same structure have been analysed (at constant azimuthal extension of 160°). The different configurations have

been named after the initial of the filling material (*a* for air groove and *m* for metal bump) starting from the bottom corrugation. As an example, the normalized near-field distributions for the configuration *amama* is reported in Figure 8. As expected, field localization is achieved under H excitation, while the V distribution maintains an almost two-lobed pattern.

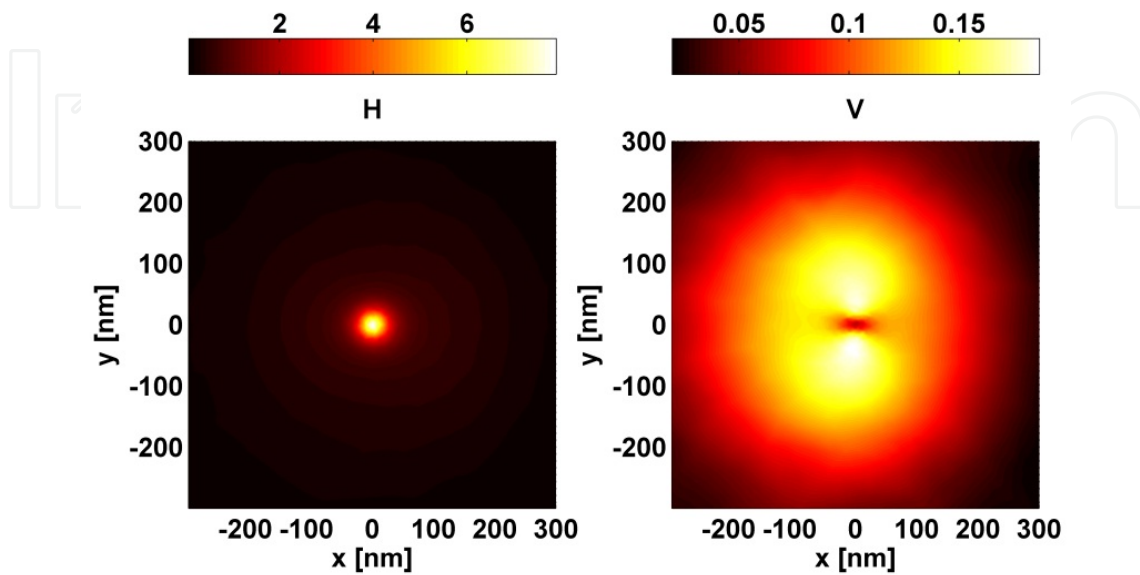


**Figure 8.** Normalized near-field intensity distributions at 10 nm from the apex of a probe with asymmetric corrugations (*amama* configuration) (adapted from [51]).

A systematic analysis of the FWHM and the peak value of the hot spot achieved under H polarized excitation for all the possible permutations of air indentations and metal bumps for the same structure has revealed that, except for only one configuration, the size of the near-field distribution undergoes a significant shrinkage in all the cases with the creation of a real ultrasmall spot in most of the cases with a FWHM comparable to that observed for the R mode excitation in the axisymmetric probe (Figure 9(a)). Although the H peak value generally increases compared to the case of the standard axisymmetric probe, only few material combinations give rise to values comparable or, in two cases, even much superior to the radial peak for the axisymmetric probe, with the best results given by the *amama* configuration (Figure 9(b)). Similar trends in terms of alternation of metal and dielectric have been observed upon replacement of the air grooves with metal oxide bumps (in this case aluminium oxide) and considering all the possible permutations of metal and metal oxide in the five semirings. However, the substitution of air with metal oxide gives rise to higher peak values due to better coupling between inner and outer SPPs when air is substituted with metal oxide, because the coupling of surface modes at two adjacent metal-dielectric interfaces becomes more efficient when the indices of refraction of the two dielectrics are closer [73].

Next, the influence of a variation of a geometric parameter, i.e. the azimuthal extension of the corrugations, has been studied. The *amama* configuration has been chosen and the angular extension of each corrugation has been changed between  $110^\circ$  to  $160^\circ$  with a step of  $10^\circ$ . No significant variations in the FWHM for the H hot spots have been observed, while the peak value increases with increasing azimuthal extension of the corrugations.

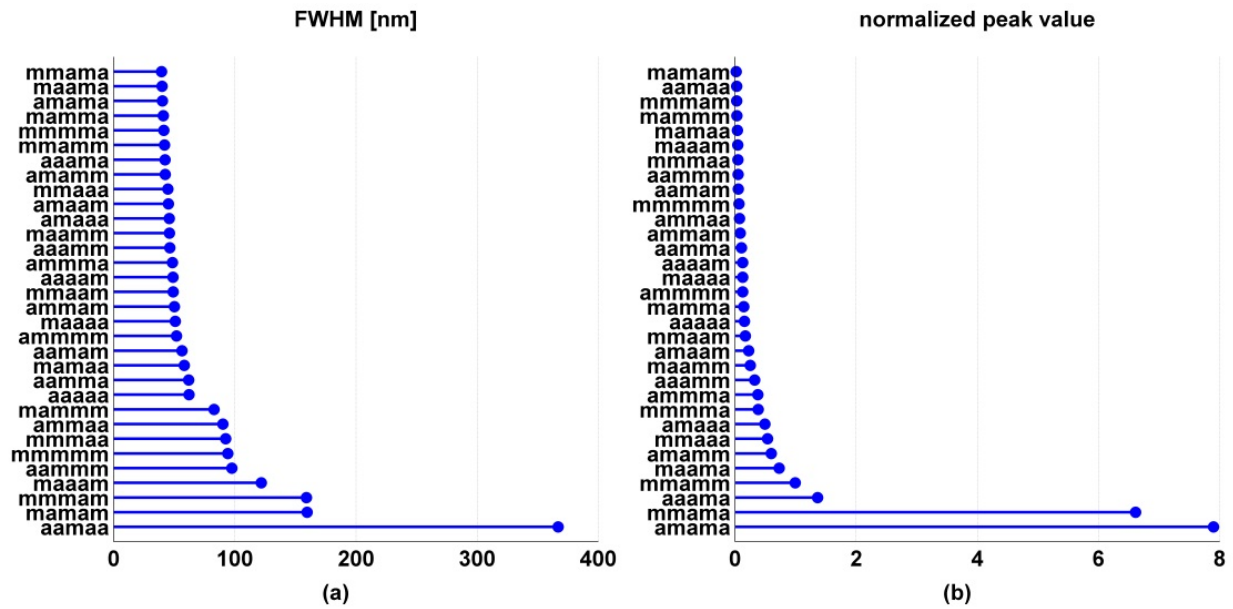


**Figure 9.** Characteristics of the near-field intensity distributions at 10 nm from the apex of the probe with asymmetric corrugations under H polarized excitation for each of the material permutations in the five semirings: (a) FWHM; (b) peak value normalized to the one achieved in an axisymmetric probe under radially polarized excitation (adapted from [51]).

### 6.3. Analysis of the behaviour of the directional asymmetries for arbitrary orientation of the asymmetry with respect to the input polarization

Our finite element based simulations have shown that carefully designed asymmetries introduced in an originally axisymmetric fully metal-coated tip can produce field localization under an excitation linearly polarized along a proper polarization direction. The presence of the asymmetry causes the electric fields associated with SPPs on the opposite sides of the tip not to have opposite phases any longer, a phenomenon that leads to destructive interference under linearly polarized injection in an axisymmetric structure [51,57]. A global analysis of the results obtained for both a cut probe and a tip with asymmetric corrugations has shown that this effect is enhanced when the asymmetry is extended over a broader region (as is the case for steeper cut angles or lower cut heights in case of the probe with oblique cut or a larger azimuthal extension of the corrugation for the tip with asymmetric corrugations). In this way, superfocusing can be achieved with a linearly polarized injection, which is much easier than a radially polarized one, with an enormous simplification in experimental applications.

However, so far we have considered the behaviour of the probe for two specific orientations of the input linearly polarized excitation with respect to the asymmetry (located along  $x$ ), i.e. alignment along the direction of the asymmetry (H polarization) or alignment along the direction orthogonal to the asymmetry (V polarization). Field localization occurs for input polarization aligned along the preferential direction of the asymmetry, while no significant variation compared to the axisymmetric probe is shown for input polarization orthogonal to such direction.

In this section, to better understand how the misalignment from the preferential spatial direction can affect the performance of a probe with a directional asymmetry, we show the behaviour of a probe based on asymmetric corrugations for variable mutual orientation of the direction of the input linearly polarized excitation with respect to the one of the asymmetry [55,57,74]. Such mutual alignment has been defined as the angle  $\alpha$  between the direction of the input linear polarization and the angle bisector of the corrugations (Figure 10(a)); the mutual orientation specified by  $\alpha$  was varied from  $-85^\circ$  to  $90^\circ$  to encompass all the possible mutual positions. Note that  $\alpha=0^\circ$  and  $\alpha=90^\circ$  correspond to  $x$  and  $y$  linearly polarized excitations so far labelled as H and V, with  $\alpha=0^\circ$  representing the position of best alignment of the input linear polarization with respect to the directional asymmetry and  $\alpha=90^\circ$  representing the maximum misalignment.

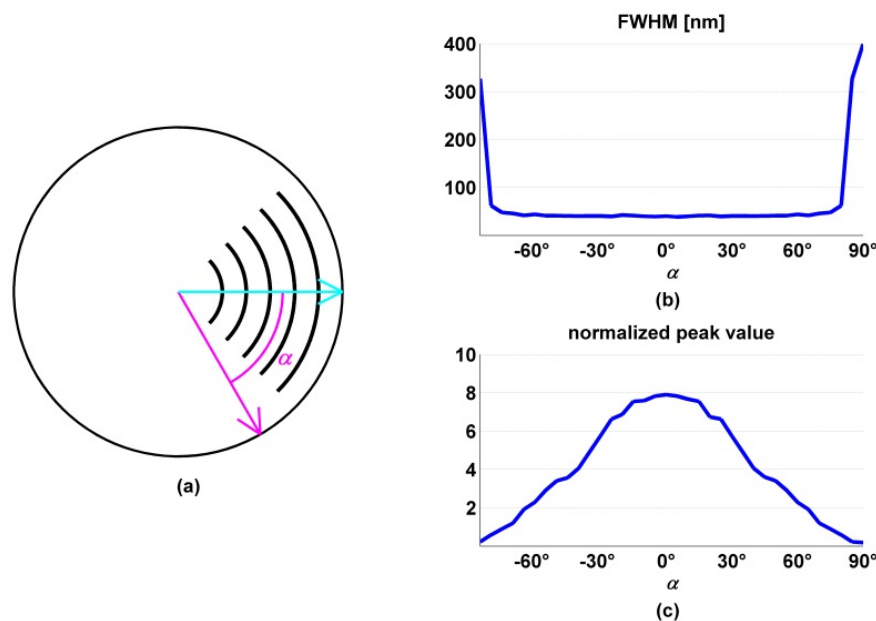


**Figure 10.** Behaviour of the probe with asymmetric corrugations for variable orientation of the input linearly polarized excitation with respect to the asymmetry: (a) schematic of the  $xy$  projection of the probe: the angle  $\alpha$  is the one between the direction of the input linear polarization (magenta line) and the angle bisector of the corrugations (cyan line); (b) FWHM of the near-field distribution for the *amama* configuration under variable  $\alpha$ ; (c) peak value of the near-field distribution normalized to the one of the axisymmetric probe under radially polarized excitation for the *amama* configuration under variable  $\alpha$  (adapted from [55]).

Figure 10 (b) and (c) report the FWHM and the normalized peak value as a function of  $\alpha$  for the *amama* configuration and azimuthal extension of the corrugations equal to  $160^\circ$ . As the misalignment of the input polarization from the preferential direction of the asymmetry increases, both the peak value and the shape of the near-field intensity pattern change. In particular, the peak value decreases and the distribution becomes gradually broader. This is due to the fact that, as  $\alpha$  increases, the asymmetry perceived by the input linearly polarized excitation progressively disappears. In retrospect, the different behaviour can be explained if recalling that a structure asymmetric along  $x$  appears symmetric for a  $y$  linearly polarized excitation, which brings about destructive

interference of the excited SPPs, similarly to what happens for an axisymmetric structure under linearly polarized excitation. If we consider the average of both the FWHM and the peak value over all the possible mutual positions, from the graphs it can be inferred that maximum deviations of the peak value and of the spot size from the corresponding averages are about 100% and 450%, respectively.

Similar analyses have been run for various forms of directional asymmetries with different structural parameters. The maximum deviation of the peak ratio and of the spot size from the average value over all the mutual orientations of the linearly polarized excitation with respect to the asymmetry is reported in order to highlight the sensitivity to mode orientation (Figure 11).

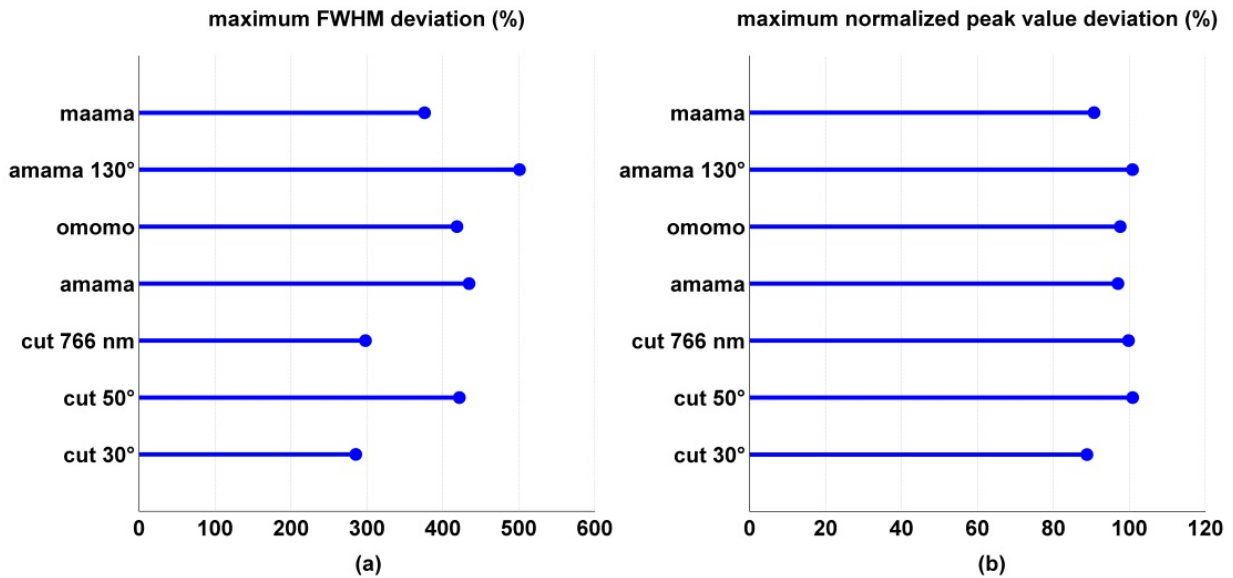


**Figure 11.** Characteristics of the near-field intensity distributions for directional asymmetries under linearly polarized excitation for variable orientation  $\alpha$  of the asymmetry with respect to the input linear polarization: (a) maximum deviation from the average FWHM; (b) maximum deviation from the average normalized peak value; *omomo* is a probe with asymmetric corrugations and alternation of oxide (*o*) and metal (*m*) bumps (adapted from [57]).

Variations in the peak value are above 90% and, more importantly, those in spot size exceed 280%. Such strong variations are due to the intrinsic directional nature of the asymmetries, with degradation in peak intensity and resolution as a consequence of misalignments from the preferential direction of the asymmetry.

## 7. Numerical investigation of probes with adirectional asymmetries under linearly polarized excitation

In order to reduce the sensitivity of the probe behaviour to the direction of the input polarization, we have introduced the concept of adirectional asymmetry. Two different implementations of this structural modification have been considered, both based on a spiral design: in fact, the spiral intrinsically fits the specification of lack of rotational and

reflection symmetry and offers an interesting case study to investigate the feasibility of the concept of orientation-insensitive field localization [55,57]. First, the effects of a spiral corrugation on the outer metal surface of a fully metal-coated probe have been investigated. Then, another implementation based on azimuthal corrugations arranged in a spiral-like fashion will be discussed. A sketch of the two structures is shown in Figure 12.

The spiral corrugation is formed by joining a tapered helix-shaped 3D object (with circular cross-section of radius  $r$ ) with two hemispherical terminations (having the same radius  $r$ ). The spiral winding appears as a semicircular spiral corrugation and is placed between 150 nm and 750 nm along the  $z$  direction; the pitch along  $z$  is 300 nm. The spiral corrugation can take on the form of either a groove, i.e. it is filled with air, or a bump, corresponding to metal filling; the effect of metal oxide filling has been analysed as well [57].

The azimuthal corrugations are formed by joining truncated toroids with hemispherical terminations as in paragraph 6. However, in order to create a spiral arrangement (and hence an adirectional asymmetry distributed over all spatial directions), the corrugations are shifted one with respect to the other [55].

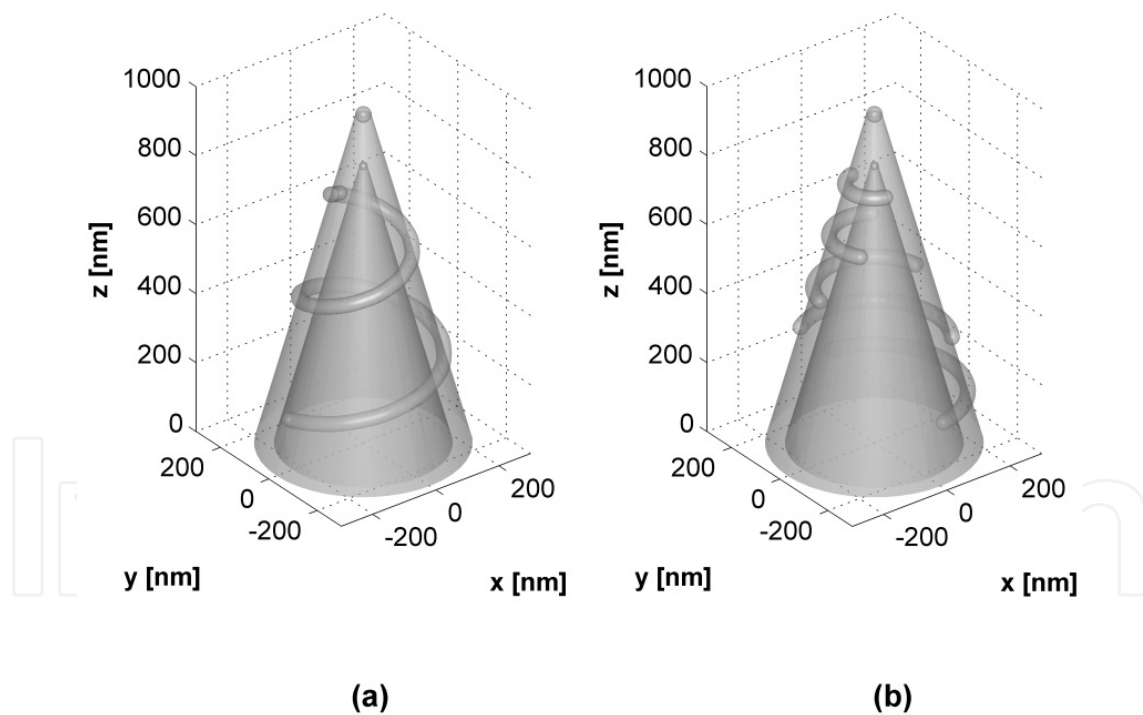


**Figure 12.** Sketch of the structures based on an adirectional asymmetry: (a) probe with spiral corrugation; (b) probe with spiral-arranged azimuthal corrugations.

### 7.1. Probe with spiral corrugation

The near field distributions obtained for a spiral metal corrugation with radius  $r = 25$  nm under H and V polarized excitation are illustrated in Figure 13.

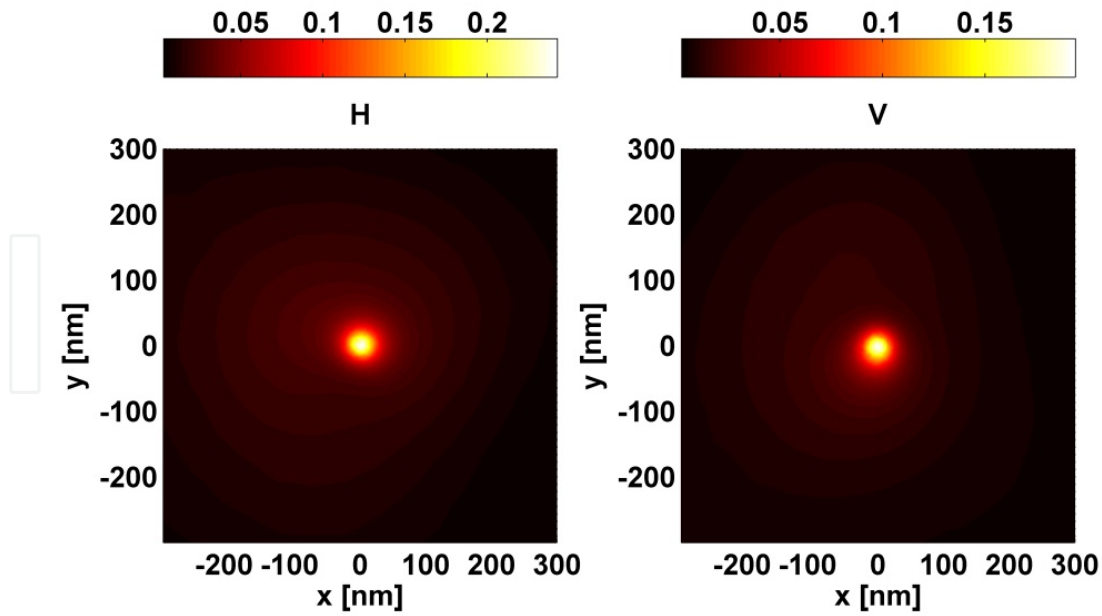


**Figure 13.** Normalized near-field intensity distributions at 10 nm from the apex of a probe with a spiral metal corrugation of radius  $r = 25$  nm (adapted from [57]).

Strong field localization is observed for both the orthogonal input polarizations, with the creation of ultrasmall spots very similar in terms of both FWHM and peak value. As illustrated below, the intensity (that, in this case, is still 5 times lower than the one of the radial hot spot of the axisymmetric probe) can be adjusted by changing either the filling material or the radius of the corrugation. Similar near-field distributions have been observed upon variation in the chirality of the spiral winding (that is whether it wraps the tip in clockwise or counter-clockwise direction).

An analysis of the FWHM and the peak value (normalized to the peak achieved in the reference axisymmetric probe under radially polarized excitation) under different mutual orientations  $\alpha$  of the direction of the linearly polarized excitation with respect to the asymmetry has been carried out to assess the properties of the adirectional asymmetry: according to Figure 14,  $\alpha=0^\circ$  corresponds to  $x$  linearly polarized excitation, with the two extremes of the spiral winding located along the  $x$  axis.

The most noticeable feature is that only minor fluctuations occur in the FWHM, which means that the spot size is almost insensitive to variations in the mutual orientation. We should remind that the FWHM is related to the eventual achievable resolution and, hence, its robustness with respect to variations in the orientation of the input polarization implies a substantial simplification in experimental applications. Although the peak value still depends on the mutual orientation, the maximum deviation from its average value calculated over all the mutual positions is below 20%, still tolerable if the average value were sufficiently high for detection. Note that, contrarily to the case of directional asymmetry where  $\alpha=0^\circ$  and  $\alpha=90^\circ$  represented the best and worst alignment, for the adirectional asymmetry different orientations are almost equivalent.

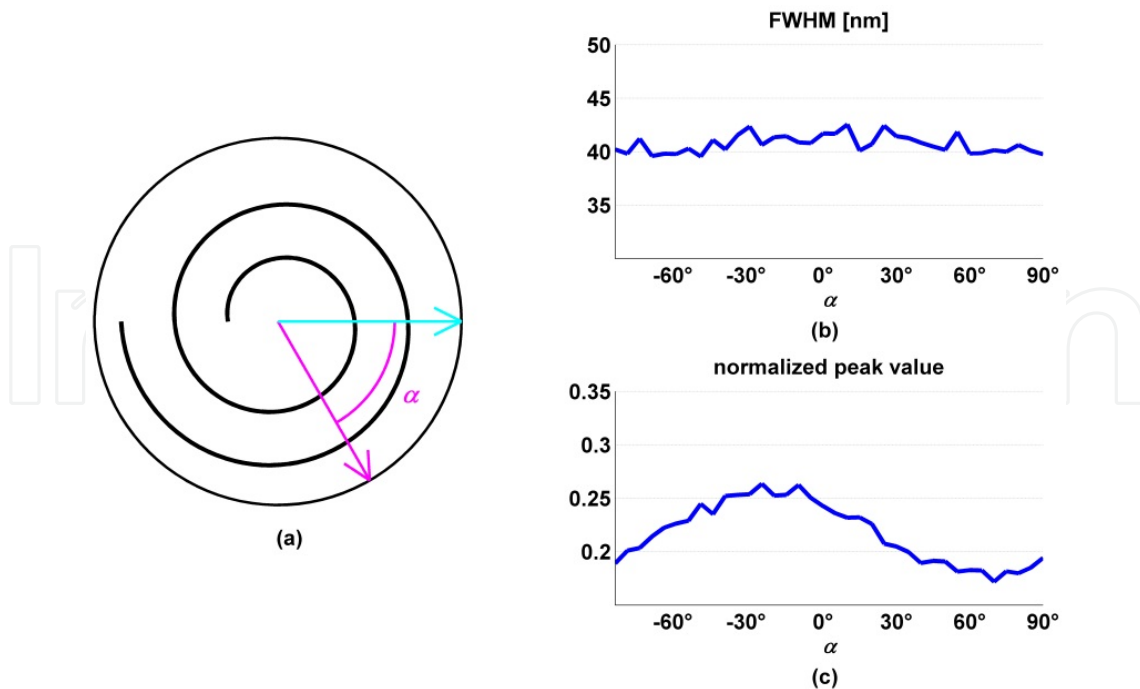


**Figure 14.** Behaviour of the probe with spiral corrugation for variable orientation of the input linearly polarized excitation with respect to the asymmetry: (a) schematic of the  $xy$  projection of the probe: the angle  $\alpha$  is the one between the direction of the input linear polarization (magenta line) and the line along which the two extremes of the spiral are aligned (cyan line); (b) FWHM of the near-field distribution for the spiral metal corrugation under variable  $\alpha$ ; (c) peak value of the near-field distribution normalized to the one of the axisymmetric probe under radially polarized excitation for the spiral metal corrugation under variable  $\alpha$  (adapted from [57]).

Similarly to the case of directional asymmetries, the FWHM and the peak value can be optimized by varying the characteristics of the spiral asymmetry. In particular, we changed the radius  $r$  of the spiral from 15 nm to 30 nm with a step of 5 nm. Moreover, we considered the case of replacement of the metal spiral bump with a spiral groove (air filling) or with an aluminium oxide spiral bump. In particular, for each structure based on a particular combination of filling material and radius  $r$ , the behaviour of the probe under all the possible mutual orientations of the linearly polarized excitation with respect to the spiral winding was examined, by calculating the average value of the peak ratio and the FWHM over all the mutual orientations and considering these values together with the maximum deviation from the corresponding average as figures of merit for comparison.

As for the directional asymmetries, overall better results (i.e. smaller spot size and higher peak values) have been obtained for stronger asymmetries due to larger  $r$  values. However, differently from the case of directional asymmetries, the data about the maximum deviation confirm that field localization is achieved irrespective of the mutual orientation between the linearly polarized mode and the asymmetry introduced in the structure. The deviation in FWHM dips as the radius increases, while the peak value shows an opposite trend with a change of the spiral radius: however, the maximum deviations are still acceptable, especially if combined with a rise in the average value occurring when the metal bump is substituted with an air groove or, even better, an aluminium oxide bump. The behaviour of the probe as

a function of the filling material can be explained as a result of better coupling mechanisms between inner and outer SPPs, as also pointed out in paragraph 6.2.

## 7.2. Probe with corrugations arranged in a spiral-like fashion

The spiral corrugation can be replaced by a series of azimuthal corrugations shifted one with respect to the other to create a spiral arrangement, as visible in the 2D projection of Figure 15; the angle  $\alpha$  between the direction of the input linearly polarized excitation and the angle bisector of the bottom corrugation is also defined. The parameters of this new structure can be varied to improve the field localization and enhancement for any orientation of the input linearly polarized excitation.

The effect of variations in the shift angle  $\beta$  (identical for any two consecutive corrugations) has been examined as well as the impact of variable radius and variable azimuthal extension  $\gamma$  of the single corrugations (which means the arc of circumference over which corrugations are spanned). According to the sketches in Figure 12 and Figure 15, the angle bisector of the bottom corrugation is along the  $x$  axis. The  $z$  spacing between consecutive corrugations, which can be either grooves or bumps, is 150 nm. We focused our attention on the structure based on alternation of grooves and bumps starting from the bottom corrugation, previously labelled as *amama*, because the studies reported in paragraph 6.2 for null shift angle  $\beta$  between consecutive corrugations showed that it resulted in the best performance.

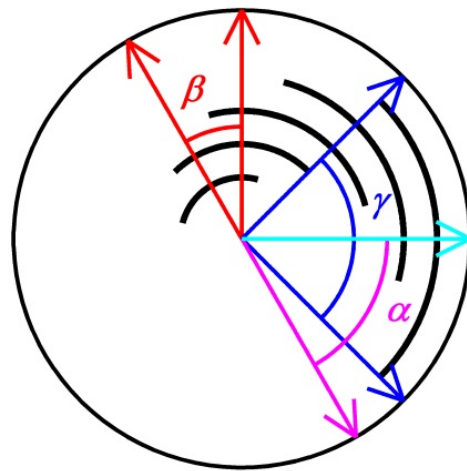


**Figure 15.** Schematic of the 2D projection of the probe with spiral-arranged corrugations and relevant parameters; the black arcs represent the corrugations; the angle  $\alpha$  is the one between the direction of the input linear polarization (magenta line) and the angle bisector of the bottom corrugation (cyan line); the angle  $\beta$  is the shift angle measured between the angle bisectors of two consecutive corrugations, while the angle  $\gamma$  is the angular extension of each corrugation. The angle bisector of the bottom corrugation is along the  $x$  axis (adapted from [55]).

Figure 16 reports the square of the normalized near field distributions under H and V polarized excitation for a shift angle  $\beta$  of  $45^\circ$  (adirectional asymmetry), total azimuthal extension  $\gamma$  for each of the five corrugations equal to  $160^\circ$  and radius of 20 nm. The two distributions show close resemblance in both peak value and FWHM.

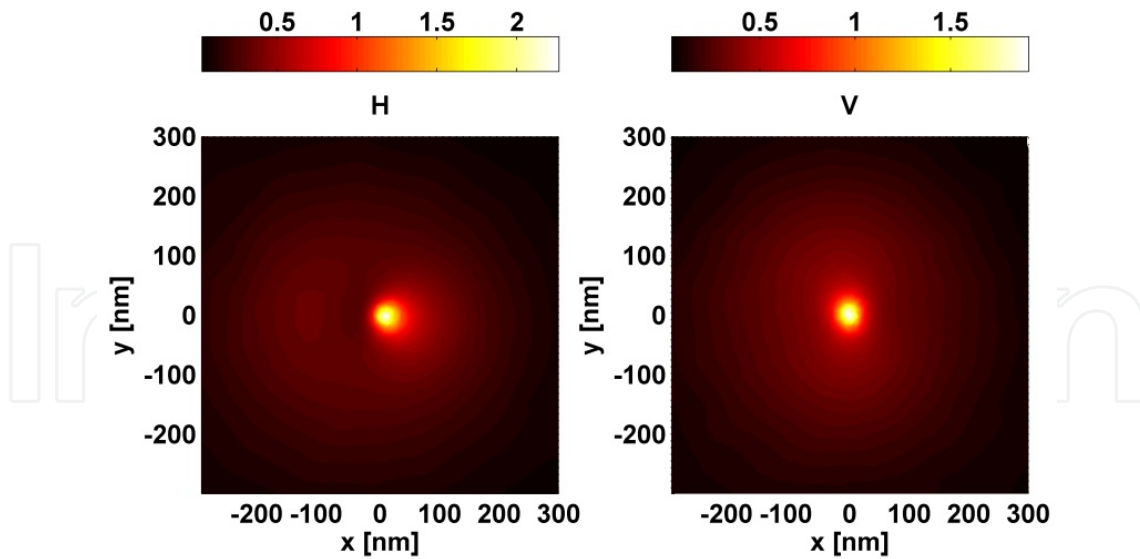


**Figure 16.** Normalized near-field intensity distributions at 10 nm from the apex of a probe with azimuthal corrugations arranged in a spiral-like fashion ( $\beta=45^\circ$ ;  $\gamma=160^\circ$ ; radius 20 nm) (adapted from [55]).

In order to further confirm that field localization is insensitive to the alignment of the input polarization, also for this asymmetry we studied the behaviour of the probe under variable orientation of the corrugations with respect to the input linear polarization, and, in particular, the FWHM and the peak value normalized to the one of the axisymmetric probe under radially polarized excitation.

Figure 17 shows deviations of the peak value from the average below 20% and those of the spot size less than 10% for the probe with adirectional asymmetry, which demonstrates the possibility to get superfocusing under arbitrarily oriented linearly polarized excitation. In particular, the ultimate achievable resolution is almost insensitive to the input polarization direction. Similar trends were observed by changing the chirality, i.e. the handedness, of the spiral-like arrangement.

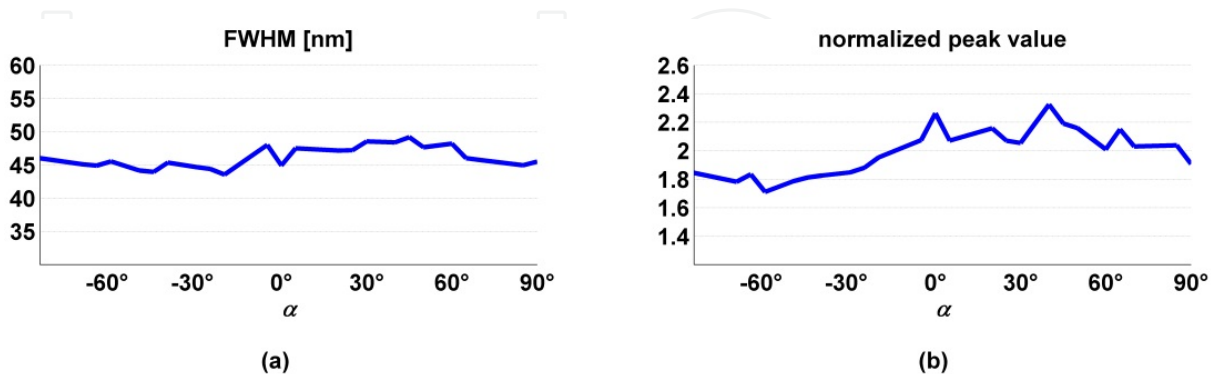


**Figure 17.** Behaviour of the probe with spiral-arranged corrugations for variable orientation  $\alpha$  of the input linearly polarized excitation with respect to the asymmetry ( $\beta=45^\circ$ ;  $\gamma=160^\circ$ ; radius 20 nm): (a) FWHM of the near-field distribution for variable  $\alpha$ ; (b) peak value of the near-field distribution normalized to the one of the axisymmetric probe under radially polarized excitation for variable  $\alpha$  (adapted from [55]).

The effect of some geometric parameters (more specifically the shift angle  $\beta$ , the angular extension  $\gamma$  and the radius of the corrugation) on the probe behaviour has been analysed as well. By increasing the shift angle from  $0^\circ$  to  $45^\circ$  (with a step of  $7.5^\circ$ ), a better confinement and an increase in the peak value has been observed, together with smaller variations in these parameters under variable orientation of the corrugations with respect to the input linearly polarized excitation. An increase in the angular extension and in the radius has also been shown to have an overall beneficial effect on probe behaviour.

## 8. Interaction of asymmetric probes with fluorescent molecules

Beyond the overall intensity distribution, also the analysis of the single vectorial components of the near-field distribution is of major interest and provides insight into the field localization mechanisms. A full vectorial picture of the electric field distribution close to the tip apex can be gained by scanning single fluorescent molecules with a SNOM probe. In the seminal work by Betzig and Chichester, the near-field distribution of aperture probes was mapped by fluorescent molecules, which act as point detectors for the components of the electric field aligned along their absorption dipole direction [75]. The interaction of single fluorescent molecules with aperture probes has been thoroughly investigated both experimentally and theoretically, not only as a tool for probe characterization, but also for its importance in biological as well as in material science [60,76-78].

For all these reasons, we have investigated the interaction of a single fluorescent molecule with an axisymmetric probe under radially polarized excitation and with an asymmetric probe under linearly polarized excitation in order to identify the similarities between the vectorial components of the near-field distributions close to the apex of the probes [79]. In most of the calculations, we considered the cut probe as an example of asymmetric probe due to the simplicity to fabricate this probe using FIB milling, as will be discussed in the next paragraph.

Figure 18 shows the quantities necessary to describe the dipole moment of the fluorescent molecules.

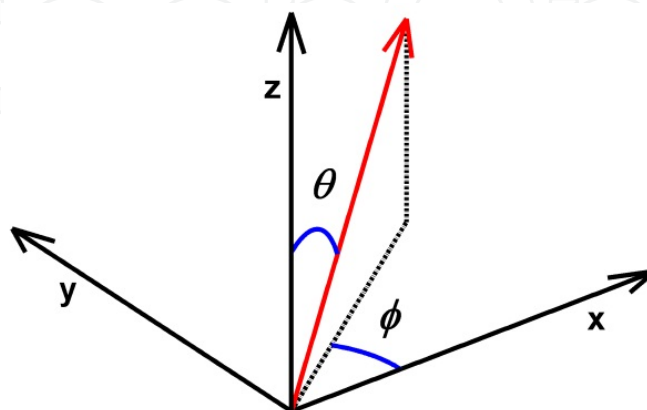


**Figure 18.** Representation of the orientation of the dipole (red vector) through the polar angle  $\theta$  and the azimuthal angle  $\phi$ .

The fluorescence intensity  $I$  emitted by a molecule is related to the square of the dot product of the local electric field  $E$  and the normalized absorption dipole moment  $p$  far from saturation [75]:

$$I \propto |E \cdot p|^2 \quad (4)$$

Therefore, the fluorescence intensity  $I$  depends on both the absolute value and the direction of the electric field, which shows the ability of a fluorescent molecule to provide a vectorial picture of the local electric field. The normalized absorption dipole moment describing the 3D dipole orientation is given by:

$$p = \begin{pmatrix} \sin \theta \cos \phi \\ \sin \theta \sin \phi \\ \cos \theta \end{pmatrix} \quad (5)$$

where  $\theta$  and  $\phi$  represent the polar and azimuthal angle, respectively (Figure 18). In our case the local field  $E=(E_x, E_y, E_z)$  coincides with the electric field distribution on the  $xy$  plane at a distance  $z$  of 10 nm above the probe apex.

The interaction of an axisymmetric probe under radially polarized excitation with a fluorescent molecule with polar and azimuthal orientation varying from  $0^\circ$  to  $90^\circ$  (with a step of  $30^\circ$ ) was considered. The resulting fluorescence intensity distributions calculated according to equation (4) on a 400 nm by 400 nm square area centered on the probe apex are shown in Figure 19, with an indication of the peak intensity for a molecule with a specific dipole orientation normalized to the peak of the total local electric field intensity  $|E|^2$  (number reported in white). As visible, the radially polarized excitation gives rise to a strong longitudinal local field at the tip apex (aligned along the probe axis  $z$  and corresponding to  $\theta=0^\circ$ ), made up of a single hot spot, and weaker orthogonal transverse components (corresponding to  $\theta=90^\circ$  and  $\phi=0^\circ$  and  $\theta=90^\circ$  and  $\phi=90^\circ$ , respectively) of almost equal magnitude appearing as two-lobed patterns.

A variation in the azimuthal angle of the fluorophore corresponds to almost identical intensity distributions, simply rotated according to  $\phi$ , because of the axial symmetry of both the probe and the input excitation. On the contrary, a decrease in the peak intensity and a gradual transition from a single spot to a two-lobed distribution occurs upon a change of the polar angle  $\theta$  from  $0^\circ$  to  $90^\circ$ , because of the overlap of the dipole absorption moment dominantly with the weaker transverse components of the local electric field rather than with the stronger longitudinal component.

The most remarkable feature is the dominance of a strong longitudinal field component, which can be beneficial for the imaging of molecules with a mainly longitudinal dipole moment. Moreover, molecules with identical polar angle and different azimuthal orientation give rise to similar fluorescent patterns apart from the rotation by  $\phi$ , which allows the determination of the azimuthal component of the fluorophore dipole moment. On the

contrary, using aperture probes, molecules with variable azimuthal angle result in strongly different patterns due to the significant differences in orthogonal transverse components close to the aperture, with variations in peak intensities by even two orders of magnitude [77].

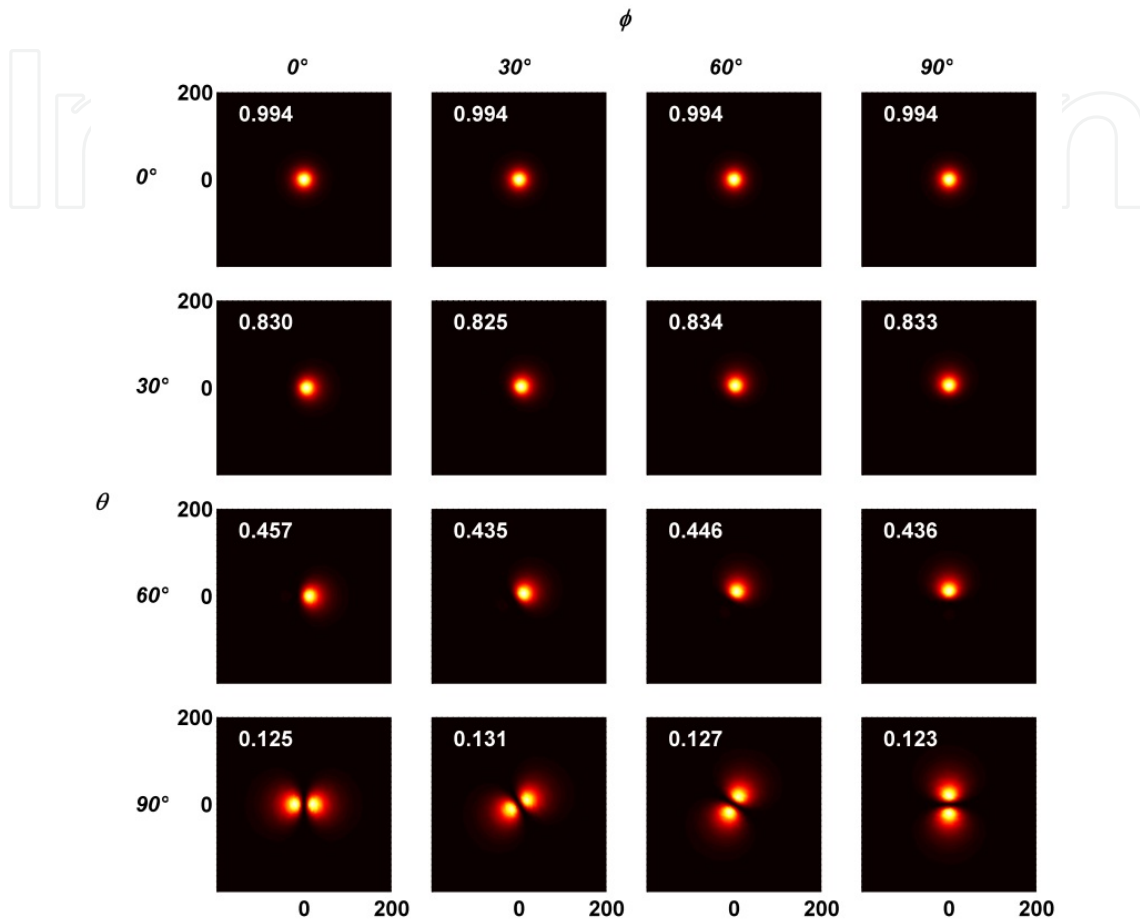


**Figure 19.** Simulated fluorescence intensity maps for single molecules with different orientations (as specified by the polar angle  $\theta$  and the azimuthal angle  $\phi$ ) excited by an axisymmetric fully metal-coated probe under radially polarized excitation and located at 10 nm from the tip apex. All the maps are reported on the same colour scale, with each plot normalized to its peak intensity value (adapted from [79]).

A similar analysis has been run for a cut probe. Figure 20 shows the fluorescence intensity maps for a structure with a cut angle of  $30^\circ$  and a cut height of 766 nm under  $x$  linearly polarized excitation (i.e. oriented along the direction of the asymmetry;  $\alpha=0^\circ$ ). Also in this case, the dominance of the longitudinal component is clearly visible, with double-lobed orthogonal transverse components slightly different in magnitude. The close resemblance with the fluorescence distributions obtained for an axisymmetric probe under radially polarized excitation is significant, which makes the asymmetric structure eligible to replace axisymmetric probes in single fluorescent molecule studies, because the advantages pointed out for the axisymmetric probe can be obtained under an easier linearly polarized excitation.

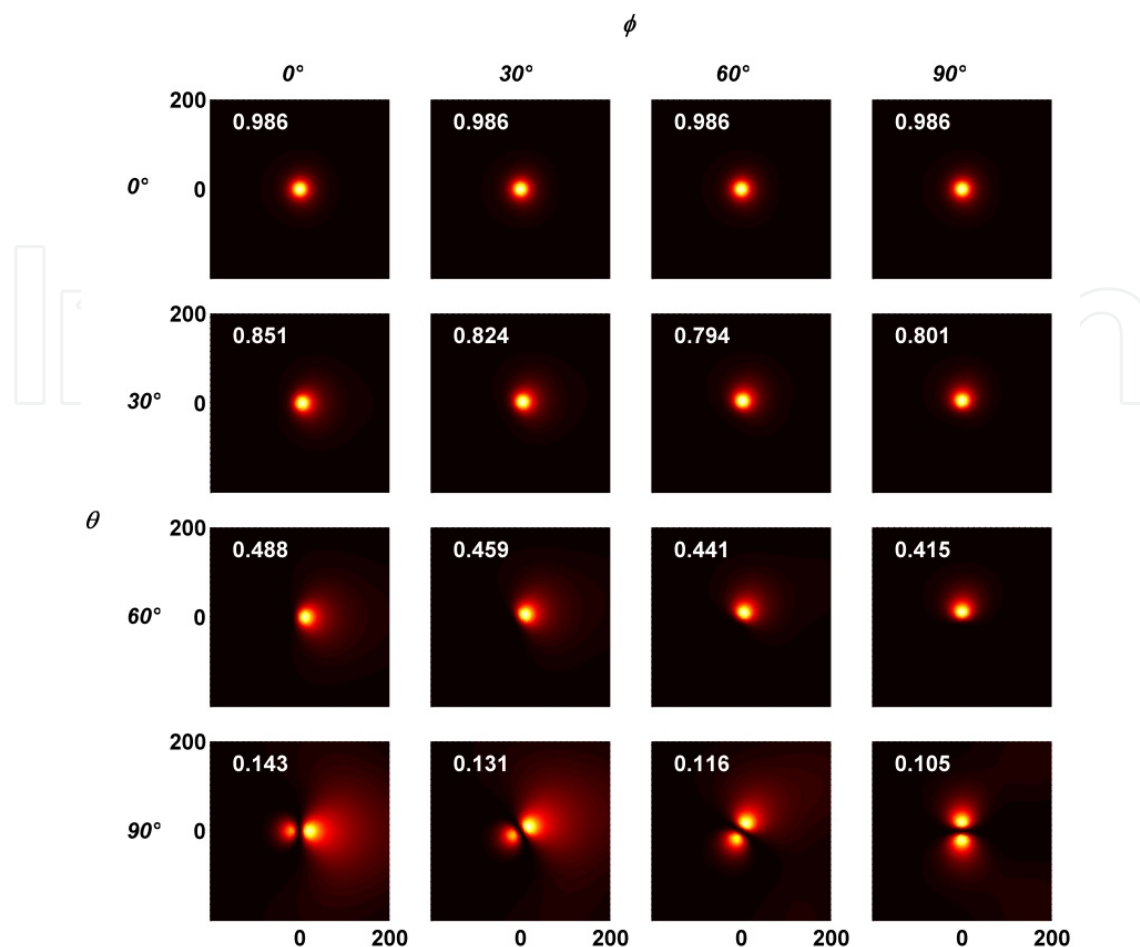


**Figure 20.** Simulated fluorescence intensity maps for single molecules with different orientations (as specified by the polar angle  $\theta$  and the azimuthal angle  $\phi$ ) excited by a cut probe under linearly polarized excitation along the direction of the asymmetry ( $x$ ) and located at 10 nm from the tip apex. All the maps are reported on the same colour scale, with each plot normalized to its peak intensity value (adapted from [79]).

The study of the interaction of different asymmetric probe structures with fluorescent molecules has revealed that all the asymmetric structures exhibit a highly confined strong longitudinal electric field component and weaker transverse components, like the axisymmetric probe under radially polarized excitation.

Moreover, the analysis of the intensity maps obtained for a fluorescent molecule with longitudinal dipole moment under variable  $\alpha$  using either the previously considered cut probe or a probe with two-turn spiral corrugation in form of an aluminium bump with 25 nm radius (as in paragraph 7.1) has confirmed once again how adirectional asymmetries are more robust to variations in the direction of the input polarization compared to the directional ones. If the asymmetry lies along one specific spatial direction, alignment of the input linearly polarized excitation with respect to the asymmetry is still necessary. On the contrary, light funnelling to a highly confined mainly longitudinally polarized distribution independent of the orientation of the input linear polarization can be achieved by extending the asymmetry over all the spatial directions.

## 9. Hints on probe fabrication

In the introduction, we have briefly summarized the fundamental steps to create an aperture fiber probe. Our modified asymmetric probes can still benefit from this well developed technology. The overall fabrication process consists in the creation of the taper and subsequent metallization. Next, the desired modification is introduced by FIB milling. In our case, for first tests on the fabrication of our novel asymmetric probes, fiber-based SNOM tips have been bought and properly modified using a dual beam FIB/SEM (scanning electron microscope) system (FEI Strata DB 235). The system includes an ion beam and an electron beam column tilted one with respect to the other by  $52^\circ$ , allowing simultaneous nanostructuring and imaging of the probe.

FIB milling has been applied in the past to the fabrication of apertures in aperture SNOM probes, either to improve the quality of apertures created by some other method or to create an aperture in a fully metal-coated probe. Two different approaches have been used for this purpose, i.e. head-on drilling and slicing [80,81]. In the first approach the  $\text{Ga}^+$  beam is scanned from the top across the tip surface using a previously generated pattern (the ion beam is aligned along the tip axis); although in this way a better control over shape and size of the aperture can be achieved by choosing an appropriate milling pattern, deep drilling into the tip structure can occur and the ion beam needs to be guided to the center of the tip apex [80-82]. In the second approach, the metal-coated fiber probe is sliced off transversally, i.e. the ion beam is incident at  $90^\circ$  with respect to the probe axis; the size of the aperture can be controlled only indirectly by estimating the correct location for slicing and the size of the milled area; small beam sizes are used to remove thin slices of material corresponding to low ion currents [80,81,83-85].

The slicing approach, properly adapted, is suitable for the fabrication of our probes based on an oblique cut. However, differently from the case of conventional aperture probes, the angle of incidence of the ion beam with respect to the probe axis is no longer  $90^\circ$ , but needs to be chosen according to the desired cut angle. The definition of cut angle corresponds to the one given in paragraph 6: hence, a simple aperture probe would correspond to a cut angle of  $0^\circ$ .

The fiber probes used to fabricate and test the probe based on an oblique cut, bought from Lovalite, have been produced by heating and pulling and subsequent deposition of aluminium. For the fabrication, a step-by-step procedure was adopted in which a milling step consisting in scanning the ion beam over a small rectangular area to remove as little material as possible was followed by an imaging step in order to check the results of the previous nanostructuring step. To get a first knowledge of the aperture size and metal thickness, first simple aperture probes with diameters between about 70 nm and 200 nm were realized. Then cut probes were produced. Figure 21 shows an example of an aperture probe and of a probe with an oblique cut, with a cut angle of  $50^\circ$ .

FIB milling could also be applied for the creation of corrugations, even a spiral one: in fact, spiral lenses have been fabricated on planar structures [86,87]. In the wake of these encouraging results, we are confident that a spiral conical corrugation could be produced as well.

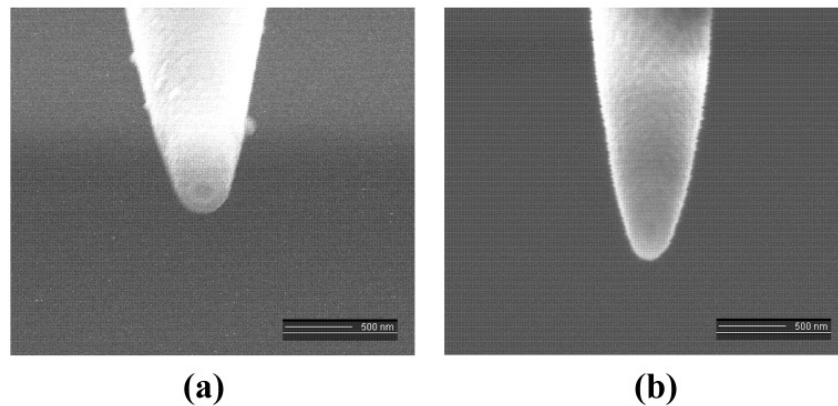


**Figure 21.** SEM image of: (a) aperture probe; (b) cut probe.

## 10. Conclusions

An extensive analysis of nanofocusing in asymmetric SNOM probe structures has been presented. The introduction of an asymmetry in an originally axisymmetric fully metal-coated probe structure has been shown to be effective in the achievement of field localization under linearly polarized excitation. In fact, in an apertureless axisymmetric structure, field localization, essential for high-resolution applications, can be attained only under radially polarized excitation. In this case, the surface plasmons excited by the radially polarized waveguide mode interfere constructively at the tip apex leading to the creation of an ultrasmall hot spot. On the contrary, those excited by a linearly polarized mode interfere destructively producing a broad, weak and asymmetric near-field distribution. However, the promising radially polarized excitation requires complicated injection procedures, extremely sensitive to misalignments.

Breaking the symmetry of the probe can help to avoid the destructive interference occurring under linearly polarized excitation allowing field localization at the tip apex under a more straightforward input excitation. Depending on the characteristics of the asymmetry, we have distinguished two different categories of asymmetry, which we called directional and adirectional asymmetries. Both the asymmetries break the axial symmetry of the original probe. However, the directional asymmetry consists in an asymmetry along one specific spatial direction; more specifically the structural modification exhibits a plane of symmetry. The adirectional asymmetry is devoid of reflection symmetry. In the first case, field localization is expected under linearly polarized excitation along the preferential spatial direction; in the second case, the field localization effect is almost insensitive to the direction of the input linearly polarized excitation. Hence, although both the categories of asymmetry obviate the need for a radially polarized excitation, adirectional asymmetries waive any requirement on the input polarization, with a further simplification of experimental procedures.

Probe design and modelling has been carried out adopting a numerical approach based on the finite element method. Two different implementations of directional asymmetries (a probe based on an oblique cut and one on asymmetric corrugations on the external metal

coating) have been considered as well as two different configurations of the pioneering adirectional probe design (a probe with a spiral corrugation and one with azimuthal corrugations arranged in a spiral-like fashion). A 3D analysis of mode propagation has confirmed that properly tailored asymmetries can bring about field localization effects under linearly polarized excitation comparable to those achieved in an axisymmetric probe under radially polarized excitation. Moreover, the adirectional design guarantees more robustness against variations in the input polarization direction. Structural parameters can be optimized to get better near-field distributions in terms of FWHM and peak value. In general, probes with more extended asymmetries have shown to result in better overall performance.

The fabrication of the modified structures can benefit from well-established technologies for probe fabrication. In particular, the asymmetry itself can be introduced using FIB nanostructuring, as shown, for example, for the probe with an oblique cut. In this case, the slicing approach, already used for the creation of aperture probes, has been properly adapted for the creation of the novel probe.

In conclusion, these new promising probe concepts could result in significant headways towards high-resolution SNOM applications.

## Author details

Valeria Lotito\*

*Electronics/Metrology Laboratory, Empa,*

*Swiss Federal Laboratories for Materials Science and Technology, Dübendorf, Switzerland*

*Department of Information Technology and Electrical Engineering, ETH Zurich, Zurich, Switzerland*

Christian Hafner

*Department of Information Technology and Electrical Engineering, ETH Zurich, Zurich, Switzerland*

Urs Sennhauser

*Electronics/Metrology Laboratory, Empa,*

*Swiss Federal Laboratories for Materials Science and Technology, Dübendorf, Switzerland*

Gian-Luca Bona

*Direction, Empa,*

*Swiss Federal Laboratories for Materials Science and Technology, Dübendorf, Switzerland*

*Department of Information Technology and Electrical Engineering, ETH Zurich, Zurich, Switzerland*

## Acknowledgement

The authors gratefully acknowledge the support of the Swiss National Science Foundation (project number 200021-115895) and the contribution of Dr. Konstantins Jefimovs (Empa) for probe nanostructuring.

---

\*Corresponding Author

## 11. References

- [1] Novotny L, Hecht B. Principles of Nano-Optics. New York: Cambridge University Press; 2006.
- [2] Hecht B, Sick B, Wild U, Deckert V, Zenobi R, Martin O, Pohl D. Scanning near-field optical microscopy with aperture probes: fundamentals and applications. *Journal of Chemical Physics* 2000;112 7761-7774.
- [3] Lewis A, Isaacson M, Harootunian A, Muray A. Development of a 500 Å spatial resolution light microscope. *Ultramicroscopy* 1984;13 227-231.
- [4] Pohl DW, Denk W, Lanz M. Optical stethoscopy: Image recording with resolution  $\lambda/20$ . *Applied Physics Letters* 1984;44 651-653.
- [5] Ambrosio A, Fenwick O, Cacialli F, Micheletto R, Kawakami Y, Gucciardi PG, Kang DJ, Allegrini M. Shape dependent thermal effects in apertured fiber probes for scanning near-field optical microscopy. *Journal of Applied Physics* 2006;99 084303.
- [6] La Rosa AH, Yakobson BI, Hallen HD. Origins and effects of thermal processes on near-field optical probes. *Applied Physics Letters* 1995;67(18) 2597-2599.
- [7] Gucciardi PG, Colocci M, Labardi M, Allegrini M. Thermal-expansion effects in near-field optical microscopy fiber probes induced by laser light absorption. *Applied Physics Letters* 1999;75(21) 3408-3410.
- [8] Novotny L, Hafner C. Light propagation in a cylindrical waveguide with a complex metallic dielectric function. *Physical Review E* 1994;50 4094-4106.
- [9] Antosiewicz TJ, Marciniak M, Szoplik T. On SNOM resolution improvement. In: Sibilica C, Benson TM, Marciniak M, Szoplik T (eds.) *Photonic crystals: physics and technology*. Milan: Springer; 2008 p. 217–238.
- [10] Saiki T, Matsuda K. Near-field optical fiber probe optimized for illumination-collection hybrid mode operation. *Applied Physics Letters* 1999;74(19) 2773-2775.
- [11] Yatsui T, Kouroggi M, Ohtsu M. Increasing throughput of a near-field optical fiber probe over 1000 times by the use of a triple-tapered structure. *Applied Physics Letters* 1998;73(15) 2090-2092.
- [12] Mononobe S, Saiki T, Suzuki T, Koshihara S, Ohtsu M. Fabrication of a triple-tapered probe for near-field optical microscopy in UV region based on selective chemical etching of a multistep index fiber. *Optics Communications* 1998;146 45-48.
- [13] Nakamura H, Sato T, Kambe H, Sawada K, Saiki T. Design and optimization of tapered structure of near-field fibre probe based on finite-difference time-domain simulation. *Journal of Microscopy* 2001;202(1) 50-52.
- [14] Yatsui T, Kouroggi M, Ohtsu M. Highly efficient excitation of optical near-field on an apertured fiber probe with an asymmetric structure. *Applied Physics Letters* 1997;71(13) 1756-1758.
- [15] Garcia-Parajo M, Tate T, Chen Y. Gold-coated parabolic tapers for scanning near-field optical microscopy: fabrication and optimisation. *Ultramicroscopy* 1995;61 155-163.
- [16] Arslanov NM. The optimal form of the scanning near-field optical microscopy probe with subwavelength aperture. *Journal of Optics A: Pure and Applied Optics* 2006;8(3) 338-344.
- [17] Bakunov MI, Bodrov SB, Hangyo M. Intermode conversion in a near-field optical fiber probe. *Journal of Applied Physics* 2004;96(4) 1775-1780.

- [18] Antosiewicz TJ, Szoplik T. Corrugated metal-coated tapered tip for scanning near-field optical microscope. *Optics Express* 2007;15(17) 10920–10928.
- [19] Wang Y, Wang Y-Y, Zhang X. Plasmonic nanograting tip design for high power throughput near-field scanning aperture probe. *Optics Express* 2010;18(13) 14004-14011.
- [20] Matteo JA, Fromm DP, Yuen Y, Schuck PJ, Moerner WE, Hesselink L. Spectral analysis of strongly enhanced visible light transmission through single C-shaped nanoapertures. *Applied Physics Letters* 2004;85(4) 648-650.
- [21] Jin EX, Xu X. Finite-difference time-domain studies on optical transmission through planar nano-apertures in a metal film. *Japanese Journal of Applied Physics* 2004;43(1) 407-417.
- [22] Danzebrink HU, Dziomba T, Sulzbach T, Ohlsson O, Lehrer C, Frey L. Nano-slit probes for near-field optical microscopy fabricated by focused ion beams. *Journal of Microscopy* 1999;194(2/3) 335-339.
- [23] Butter JYP, Hecht B. Aperture scanning near-field optical microscopy and spectroscopy of single terrylene molecules at 1.8 K. *Nanotechnology* 2006;17 1547-1550.
- [24] Tanaka K, Tanaka M. Optimized computer-aided design of I-shaped subwavelength aperture for high intensity and small spot size. *Optics Communications* 2004;233 231-244.
- [25] Minh PN, Ono T, Tanaka S, Esashi M. Spatial distribution and polarization dependence of the optical near-field in a silicon microfabricated probe. *Journal of Microscopy* 2001;202(1) 28-33.
- [26] Bortchagovsky E, Colas des Francs G, Naber A, Fischer UC. On the optimum form of an aperture for a confinement of the optically excited electric near field. *Journal of Microscopy* 2008;229(2) 223-227.
- [27] Li Z-B, Zhou W-Y, Kong X-T, Tian J-G. Polarization dependence and independence of near-field enhancement through a subwavelength circle hole. *Optics Express* 2010;18(6) 5854-5860.
- [28] Li Z-B, Zhou W-Y, Kong X-T, Tian J-G. Near-field enhancement through a single subwavelength aperture with gaps inside. *Plasmonics* 2011;6(1) 149-154.
- [29] Bouhelier A, Novotny L., Near field optical excitation and detection of surface plasmons. In Brongersma ML, Kik PG (eds.) *Surface Plasmon Nanophotonics*, Dordrecht The Netherlands: Springer; 2007 p. 139-153.
- [30] Hartschuh A. Tip-enhanced near-field optical microscopy. *Angewandte Chemie International Edition* 2008;47 8178-8191.
- [31] Stockman MI. Nanofocusing of optical energy in tapered plasmonic waveguides. *Physical Review Letters* 2004;93(13) 137404.
- [32] Babadjanyan AJ, Margaryan NL, Nerkararyan KV. Superfocusing of surface polaritons in the conical structure. *Journal of Applied Physics* 2000;87(8) 3785-3788.
- [33] Kurihara K, Otomo A, Syouji A, Takahara J, Suzuki K, Yokoyama S. Superfocusing modes of surface plasmon polaritons in conical geometry based on the quasi-separation of variables approach. *Journal of Physics A – Mathematical and theoretical*. 2007;40(41) 12479–12503.
- [34] Vogel MW, Gramotnev DK. Optimization of plasmon nano-focusing in tapered metal rods. *Journal of Nanophotonics* 2008;2 1-17.
- [35] Ruppin R. Effect of non-locality on nanofocusing of surface plasmon field intensity in a conical tip. *Physics Letters A* 2005;340(1-4) 299-302.

- [36] Baida FI, Belkhir A. Superfocusing and light confinement by surface plasmon excitation through radially polarized beam. *Plasmonics* 2009;4(1) 51-59.
- [37] Maier SA, Andrews SR, Martín-Moreno L, García-Vidal FJ. Terahertz surface plasmon-polariton propagation and focusing on periodically corrugated metal wires. *Physical Review Letters* 2006;97 176805.
- [38] Lee JS, Han S, Shirdel J, Koo S, Sadiq D, Lienau C, Park N. Superfocusing of electric or magnetic fields using conical metal tips: effect of mode symmetry on the plasmon excitation method. *Optics Express* 2011;19(13) 12342-12347.
- [39] Ropers C, Neacsu CC, Elsaesser T, Albrecht M, Raschke MB, Lienau C. Grating-coupling of surface plasmons onto metallic tips: a nanoconfined light source. *Nano Letters* 2007;7(9) 2784-2788.
- [40] Ding W, Andrews SR, Maier SA. Internal excitation and superfocusing of surface plasmon polaritons on a silver-coated optical fiber tip. *Physical Review A* 2007;75 063822.
- [41] Janunts NA, Baghdasaryan KS, Nerkararyan KV, Hecht B. Excitation and superfocusing of surface plasmon polaritons on a silver-coated optical fiber tip. *Optical Communications* 2005;253(1-3) 118-124.
- [42] Nerkararyan K, Abrahamyan T, Janunts E, Khachatryan R, Harutyunyan S. Excitation and propagation of surface plasmon polaritons on the gold covered conical tip. *Physics Letters A* 2006;350(1-2) 147-149.
- [43] Babayan AE, Nerkararyan KV. The strong localization of surface plasmon polariton on a metal-coated tip of optical fiber. *Ultramicroscopy* 2007;107(12) 1136-1140.
- [44] Nerkararyan KV, Hakhoumian AA, Babayan AE. Terahertz surface plasmon-polariton superfocusing in coaxial cone semiconductor structures. *Plasmonics* 2008;3 27-31.
- [45] Abrahamyan T, Nerkararyan K. Surface plasmon resonance on vicinity of gold-coated fiber tip. *Physics Letters A* 2007;364(6) 494-496.
- [46] Bouhelier A, Renger J, Beversluis MR, Novotny L. Plasmon-coupled tip-enhanced near-field optical microscopy. *Journal of Microscopy* 2003;210(3) 220-224.
- [47] Chen W, Zhan Q. Numerical study of an apertureless near field scanning optical microscope probe under radial polarization illumination. *Optics Express* 2007;15(7) 4106-4111.
- [48] Liu L, He S. Design of metal-cladded near-field fiber probes with a dispersive body-of-revolution finite-difference time-domain method. *Applied Optics* 2005;44(17) 3429-3437.
- [49] Vaccaro L, Aeschimann L, Staufer U, Herzig HP, Dändliker R. Propagation of the electromagnetic field in fully coated near-field optical probes. *Applied Physics Letters* 2003;83(3) 584-586.
- [50] Tortora P, Descrovi E, Aeschimann L, Vaccaro L, Herzig HP, Dändliker R. Selective coupling of HE<sub>11</sub> and TM<sub>01</sub> modes into microfabricated fully metal-coated quartz probes. *Ultramicroscopy* 2007;107(2-3) 158-165.
- [51] Lotito V, Sennhauser U, Hafner C. Effects of asymmetric surface corrugations on fully metal-coated scanning near field optical microscopy tips *Optics Express* 2010;18(8) 8722-8734.
- [52] Nakagawa W, Vaccaro L, Herzig HP. Analysis of mode coupling due to spherical defects in ideal fully metal-coated scanning near-field optical microscopy probes. *Journal of the Optical Society of America A* 2006;23(5) 1096-1105.

- [53] Frey HG, Keilmann F, Kriele A, Guckenberger R. Enhancing the resolution of scanning near-field optical microscopy by a metal tip grown on an aperture probe. *Applied Physics Letters* 2002;81(26) 5030-5032.
- [54] Taminiau TH, Segerink FB, Moerland RJ, Kuipers L(K), van Hulst NF. Near field driving of a optical monopole antenna. *Journal of Optics A: Pure and Applied Optics* 2007;9 S315-S321.
- [55] Quong MC, Elezzabi AY. Offset-apertured near-field scanning optical microscope probes. *Optics Express* 2007;15(16) 10163-10174.
- [56] Lotito V, Sennhauser U, Hafner C, Bona G-L. Fully metal-coated scanning near-field optical microscopy probes with spiral corrugations for superfocusing under arbitrarily oriented linearly polarized excitation. *Plasmonics* 2011;6 327-336.
- [57] Lotito V, Sennhauser U, Hafner C, Bona G-L. A novel nanostructured scanning near field optical microscopy probe based on an adirectional asymmetry. *Journal of Computational and Theoretical Nanoscience* 2012;9 486-494.
- [58] Roberts A. Electromagnetic theory of diffraction by a circular aperture in a thick, perfectly conducting screen. *Journal of the Optical Society of America A* 1987;4 1970-1983.
- [59] Roberts A. Near zone fields behind circular apertures in thick, perfectly conducting screens. *Journal of Applied Physics* 1989;65 2896-2899.
- [60] Dunn RC. Near-field scanning optical microscopy. *Chemical Reviews* 1999;99 2891-2927.
- [61] Issa NA, Guckenberger R. Optical nanofocusing on tapered metallic waveguides. *Plasmonics* 2007;2 31-37.
- [62] Ohtsu M. *Progress in Nano-electro-optics III Industrial applications and dynamics of the nano-optical system*. Berlin Heidelberg: Springer; 2005.
- [63] Girard C, Dereux A. Near field optics theories *Report on Progress in Physics* 1996;59 657-699.
- [64] Girard C. Near fields in nanostructures. *Report on Progress in Physics* 2005;68 1883-1933.
- [65] Moar PN, Love JD, Laudoceur F, Cahill LW. Waveguide analysis of heat-drawn and chemically etched probe tips for scanning near-field optical microscopy. *Applied Optics* 2006;45(25) 6442-6456.
- [66] Novotny L, Pohl DW, Hecht B. Scanning near field optical probe with ultrasmall size. *Optics Letters* 1995;20 970-972.
- [67] Wang XQ, Wu S-F, Jian G-S, Pan S. The advantages of a pyramidal probe tip entirely coated with a thin metal film for SNOM. *Physics Letters A* 2003;319(5-6) 514-517.
- [68] Frey HG, Bolwien C, Brandenburg A, Ros R, Anselmetti D. Optimized apertureless optical near-field probes with 15 nm optical resolution. *Nanotechnology* 2006;17(13) 3105-3110.
- [69] Nakagawa W, Vaccaro L, Herzig HP, Hafner C. Polarization mode coupling due to metal-layer modifications in apertureless near-field scanning optical microscopy probes. *Journal of Computational and Theoretical Nanoscience* 2007;4 692-703.
- [70] Bondeson A, Rylander T, Ingelström P. *Computational Electromagnetics*. New York: Springer; 2005.

- [71] Rao SS. The finite element method in engineering. Burlington MA USA: Butterworth-Heinemann; 1999.
- [72] Lotito V, Sennhauser U, Hafner C. Finite element analysis of asymmetric scanning near field optical microscopy probes. *Journal of Computational and Theoretical Nanoscience* 2010;7 1596–1609.
- [73] Janunts NA, Nerkararyan KV. Modulation of light radiation during input into a waveguide by resonance excitation of surface plasmons. *Applied Physics Letters* 2001;79(3) 299–301.
- [74] Lotito V, Sennhauser U, Hafner C. Numerical analysis of novel asymmetric SNOM tips. *PIERS Online* 2011;7(4) 394-400.
- [75] Betzig E, Chichester RJ. Single molecules observed by near-field scanning optical microscopy *Science* 1993;262(5138) 1422-1425.
- [76] Hollars W, Dunn RC. Probing single molecule orientations in model lipid membranes with near-field scanning optical microscopy. *Journal of Chemical Physics* 2000;112(18) 7822-7830.
- [77] Veerman JA, Garcia-Parajo F, Kuipers L, van Hulst NF. Single molecule mapping of the optical field distribution of probes for near field microscopy. *Journal of Microscopy* 1999;194(2-3), 477-482.
- [78] Moerland RJ, van Hulst NF, Gersen H, Kuipers L. Probing the negative permittivity perfect lens using near-field optics and single molecule detection. *Optics Express* 2005;13(5) 1604-1614.
- [79] Lotito V, Sennhauser U, Hafner C, Bona G-L. Interaction of an asymmetric scanning near field optical microscopy probe with fluorescent molecules. *Progress In Electromagnetics Research* 2011;121 281-299.
- [80] Heinzelmann H, Freyland JM, Eckert R, Huser T, Schürmann G, Noell W, Staufer U, de Rooij NF. Towards better scanning near-field optical microscopy probes – progress and new developments. *Journal of Microscopy* 1999;194(2-3) 365-368.
- [81] Muranishi M, Sato K, Osaka S, Kikukawa A, Shintani T, Ito K. Control of aperture size of optical probes for scanning near-field optical microscopy using focused ion beam technology. *Japanese Journal of Applied Physics* 1997;36(7B), L942-L944
- [82] Lacoste T, Huser T, Prioll R, Heinzelmann H. Contrast enhancement using polarization-modulation scanning near-field optical microscopy (PM-SNOM). *Ultramicroscopy* 1998;71 333–340.
- [83] Veerman JA, Otter AM, Kuipers L, van Hulst NF. High definition aperture probes for near-field optical microscopy fabricated by focused ion beam milling. *Applied Physics Letters* 1998;72 115–3117.
- [84] Pilevar S, Edinger K, Atia A, Smolyaninov I, Davis C. Focused ion-beam fabrication of fiber probes with well-defined apertures for use in near-field scanning optical microscopy. *Applied Physics Letters* 1998;72 3133–3135.
- [85] Zhang Y, Dhawan A, Vo-Dinh T. Design and fabrication of fiber-optic nanoprobe for optical sensing. *Nanoscale Research Letters* 2011;6(18) 6 pp.
- [86] Yang S, Chen W, Nelson RL, Zhan Q. Miniature circular polarization analyzer with spiral plasmonic lens. *Optics Letters* 2009;34(20) 3047-3049.
- [87] Chen W, Abeyasinghe DC, Nelson RL, Zhan Q. Experimental confirmation of miniature spiral plasmonic lens as a circular polarization analyzer. *Nano Letters* 2010;10 2075–2079.